International Journal of Mechanical Sciences 148 (2018) 596–610

Contents lists available at ScienceDirect

International Journal of Mechanical Sciences

journal homepage: www.elsevier.com/locate/ijmecsci

Nonlinear vibration and dynamic buckling analyses of sandwich functionally graded porous plate with graphene platelet reinforcement resting on Winkler–Pasternak elastic foundation

Qingya Li, Di Wu*, Xiaojun Chen, Lei Liu, Yuguo Yu, Wei Gao*

Centre for Infrastructure Engineering and Safety (CIES), School of Civil and Environmental Engineering, The University of New South Wales, Sydney, NSW 2052, Australia

ARTICLE INFO

Keywords:
Sandwich functionally graded porous plate
Graphene platelet reinforcements
Nonlinear dynamic response
Dynamic buckling
Nonlinear dynamics

ABSTRACT

The nonlinear vibration and the dynamic buckling of a graphene platelet reinforced sandwich functionally graded porous (GPL-SFGP) plate are thoroughly investigated in this paper. The investigated GPL-SFGP plate consists of two metal face layers and a functionally graded porous core with graphene platelet reinforcement. The effects of the Winkler–Pasternak elastic foundation, thermal environment and damping are incorporated. The open-cell metal foam model is implemented to model the mechanical properties of the porous core. Axial compressive stress is applied on the GPL-SFGP plate by exerting various compressive loading speeds at one edge of the plate. Grounded on the classical plate theory, both motion and geometric compatibility equations of the plate are deduced by introducing the Von Kármán strain-displacement relationship and stress function. Both the Galerkin and the fourth-order Runge–Kutta methods are implemented to solve the governing equation of the dynamic system. Meticulously designed numerical experiments are conducted to identify the critical influential factors of the dynamic stability of the GPL-SFGP plate. The influences of loading speed, damping ratio, temperature variation, initial imperfection, elastic foundation parameters, porosity, GPL weight fraction and the dimensions of the GPL on the overall dynamic stability of the GPL-SFGP plate are evidently demonstrated.

1. Introduction

With the conspicuous advantages of high stiffness and relatively light weight, sandwich structures are extensively implemented across wide range of engineering applications such as aerospace, automotive, construction and biomedical industries [1–9]. Porous materials, such as metal foam, are prevalently employed as the core of the sandwich structures due to its excellent properties provided by light weight, heat resistance and energy dissipation reduction [10–15]. The resulting composite structures, known as the sandwich porous structures, are manufactured by connecting two thin face layers with a lightweight porous core together. In general, adopting sandwich porous structures can noticeably reduce the mass of the system while ensuring the same level of stiffness. One of the attractive applications for the sandwich porous structures is the manufacture of the prototype of the high-speed train (Fig. 1). To fulfill the high demand of the engineering industries, various theoretical and experimental researches on the static and dynamic characteristics of the sandwich porous structures have been reported [16–22].

Due to the existence of internal pores of the porous material, the stiffness of the structure is decreased when the porosity is increased. To improve the performance (i.e., maintaining relatively higher stiffness but with lighter weight) of the porous structures in engineering application, nanofillers, such as carbon nanotubes [25–28] and graphene platelets (GPLs) [29], have been introduced to reinforce the porous structures. GPLs can transfer load in a more efficient way which enhances the material strength by improving the bonding with the matrix [30–32].

The functionally graded (FG) materials, whose properties vary continuously along one or multiple directions, have demonstrated their superiority over conventional composite materials in many aspects. Extensive research works have been implemented to study the dynamic behaviors of FG material structures. Grounded on the first order shear deformation theory, Sofiyev and Kuruoglu [33] analyzed the parametric vibration of simply-supported sandwich cylindrical shell with an FG core under combined static and time dependent periodic axial compressive loads. Both uniformly distributed and FG distributed patterns were considered. Yang et al. [34] explored the buckling and the postbuckling behaviors of the GPL reinforced FG multilayer beams supported by elastic foundation. Various GPL distribution patterns were studied to obtain the optimum reinforcing effect. Sofiyev et al. [35] examined the

* Corresponding authors.
E-mail addresses: di.wu@unsw.edu.au (D. Wu), w.gao@unsw.edu.au (W. Gao).

https://doi.org/10.1016/j.ijmecsci.2018.09.020
Received 9 July 2018; Received in revised form 10 September 2018; Accepted 14 September 2018
Available online 15 September 2018

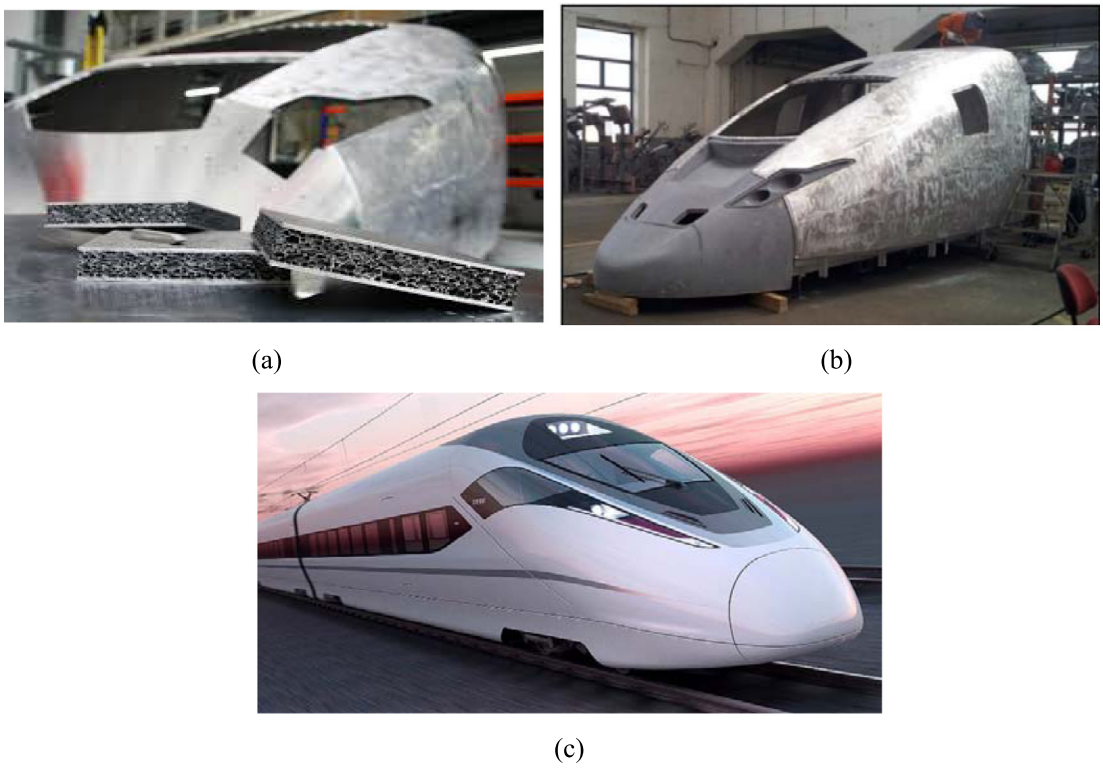

Fig. 1. (a) The sandwich porous plate; (b) Prototype of high-speed train made of welded aluminum sandwich porous structures [23]; The high-speed train [24].

dynamic response of the FG coated sandwich cylindrical shell resting on the Pasternak elastic foundation. The impacts of the shear stresses and the rotary inertia were considered.

Combining the FG composites with porous materials provides the possibility to optimize the global performance of composite structures. Several studies have investigated the vibration and bending responses of the functionally graded porous (FGP) structures. Based on the Timoshenko beam theory, Chen et al. [36] investigated the free and forced vibration characteristics of FGP beams with two different porosity distributions subjected to various loading conditions. Chen et al. [37] also adopted the Ritz method to study the nonlinear free vibration of shear deformable sandwich beam with FGP core by taking two non-uniform FG distributions into account. Wu et al. [38] proposed a finite element analysis framework to investigate the free and forced vibration of FGP beam type structures based on the Euler-Bernoulli and Timoshenko beam theories. By employing the finite element method, Chen et al. [39] investigated the dynamic response and energy absorption behaviors of 2D FGP structures with various porous distribution types. Kitipornchai et al. [40] studied the free vibration and the critical buckling load of GPL reinforced FGP beams with the considerations of three different internal pores and GPL distributions. Chen et al. [41] explored the nonlinear free vibration and postbuckling characteristics of the GPL reinforced multilayer FGP nanocomposite beams with various distribution patterns of both internal pores and GPL nanofillers. Sahmani et al. [42] investigated the size-dependent nonlinear bending of GPL reinforced FGP micro/nano-beams by employing the nonlocal strain gradient theory of elasticity and the third-order shear deformable beam theory. Yang et al. [43] employed the first-order shear deformation plate theory and Chebyshev-Ritz method to derive the buckling and free vibration behaviors of FGP nanocomposite plates reinforced by GPLs. Grounded on the first-order shear deformation theory, Dong et al. [44] investigated the free vibration behaviors of the GPL reinforced FGP nanocomposite cylindrical shell with considerations of three types of GPL patterns and four types of the porosity distributions.

It is noticed that all aforementioned researches mainly focused on the free and forced vibration of the structures. In real-life engineering application, the dynamic buckling analysis is vital to assess the safety of the structures. Aksogan and Sofiyev [45] investigated the dynamic buckling of elastic cylindrical shell with various thicknesses. The shell is subjected to a uniform external pressure as a power function of time. Deniz and Sofiyev [46] analyzed the nonlinear dynamic buckling of the FG truncated conical shells which are subjected to a linear time-dependent axial compressive load. Huang et al. [47] investigated the nonlinear dynamic buckling problem of temperature-dependent FG composite cylindrical shells subjected to a linearly increased dynamic axial load. By adopting the large deformation theory, Sofiyev [48] explored the dynamic buckling characteristics of the FG coated conical shells subjected to a time-dependent axial load. Mouhat and Abdellatif [49] presented the dynamic buckling analysis of stiffened panels subjected to an in-plane uniform axial compressive loading. With the consideration of six different boundary conditions, Azarboni et al. [50] investigated the nonlinear dynamic buckling of imperfect rectangular plate subjected to various impulsive loads. Kolahchi et al. [51] conducted the dynamic stability analysis of the single-walled CNTs reinforced polymeric temperature-dependent viscoelastic plates resting on orthotropic temperature-dependent elastomeric medium. Yang and Wang [52] presented the dynamic buckling of the stiffened plate subjected to an in-plane impact load under elastically restrained boundary conditions. Sheng et al. [53] proposed a reduction nonlinear model to investigate the dynamic stability and nonlinear vibrations of the stiffened FG cylindrical shell in thermal environment. Hajmohammad et al [54] investigated the dynamic buckling behavior of a laminated viscoelastic FG-CNT-reinforced sandwich plates. The core of the plate was made of nanocomposite layers integrated with piezoelectric materials subjected to an electric field. Gao et al. [55] analyzed the dynamic stability of a composite orthotropic plate with the consideration of damping, temperature and the Winkler–Pasternak foundation. Hajmohammad et al [56] conducted the dynamic buckling analysis of viscoelastic sandwich truncated conical shell exposed to moisture, temperature and

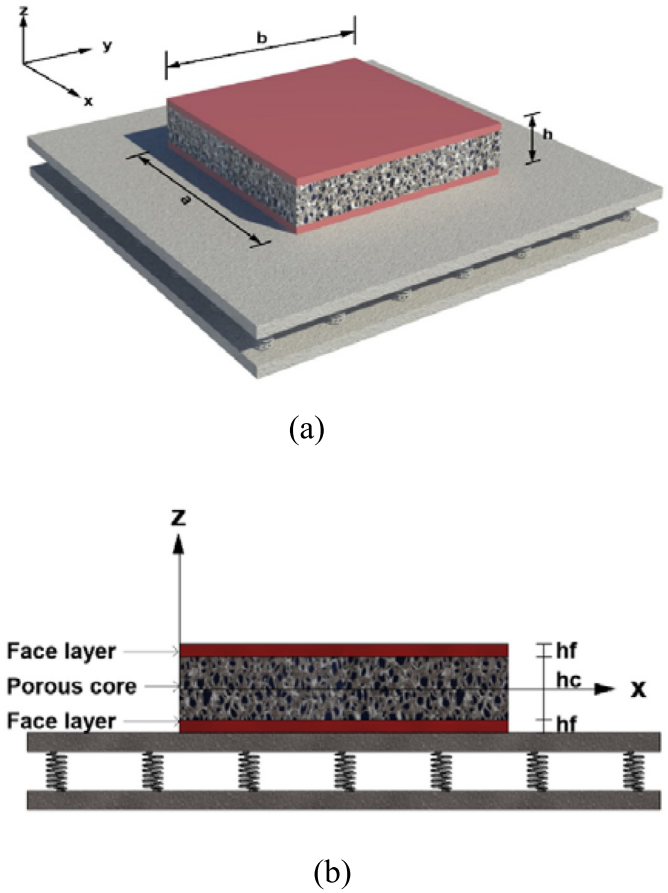

Fig. 2. (a) 3D view and (b) front view of the GPL-SFGP plate resting on the Winkler–Pasternak elastic foundation.

magnetic field. Arani et al. [57] presented the dynamic analysis of a rectangular porous plate subjected to a dynamic transverse load resting on the Pasternak foundation. Fakhar and Kolahchi [58] conducted the dynamic buckling analysis of sandwich plates with magnetorheological fluid core and piezoelectric nanocomposite face layers. Magnetic field and 3D electric field are applied on the core and the face layers respectively. However, to the best of the authors' knowledge, no previous investigation has been conducted on the dynamic stability analysis of the GPL-SFGP plate structures with the considerations of various practically motivated effects.

This paper presents an analytical approach to study the nonlinear dynamic response and buckling analysis of a graphene platelet reinforced sandwich functionally graded porous (GPL-SFGP) plate. To achieve a more generalized nonlinear dynamic analysis, the Winkler–Pasternak elastic foundation, thermal operational environmental, as well as damping effects are simultaneously incorporated. The dynamic compressive load is applied along the longitudinal direction by setting a constant displacement rate on one edge of the plate. In addition, an out-plane uniformly distributed pressure is exerted on the plate. The investigated GPL-SFGP plate in the present study possesses the mechanical properties of open-cell metal foam to obtain the porosity and mass density coefficients of the porous core. The Von Kármán strain-displacement relationship and the classical plate theory are adopted for the compatibility formulations. The Galerkin method combined with the fourth-order Runge–Kutta approach are implemented to solve the governing equation of the dynamic buckling. Furthermore, the influences of imperfections, thermal variations, external excitations, loading speeds, damping ratios, elastic foundation parameters, porosities, the GPL weight fractions as well as the GPL dimensions on the dynamic stability of the GPL-SFGP plate are evidently explored.

2. Porosity distribution and GPL patterns

A GPL-SFGP plate resting on the Winkler–Pasternak elastic foundation is defined in a Cartesian coordinate system (x, y, z), which is shown in Fig. 2. The x-y plane is defined as the middle surface of the plate, and the z-axis is indicating the thickness direction. The length, width and total thickness of the GPL-SFGP plate are denoted as a, b and $h = h_c + 2h_f$, respectively. h_c and h_f denote the thicknesses of the porous core and the metal face layer, respectively. The investigated GPL-SFGP plate is assumed to be simply supported. The uniformly distributed external pressure is exerted on the plate and an axial compressive loading rate is applied on the edge of the plate along the x-direction.

The location-dependent material properties, which are including the Young's modulus ($E(z)$), shear modulus ($G(z)$), mass density ($\rho(z)$) and thermal expansion coefficient ($\alpha(z)$) of the porous core, are described by Eqs. (1)–(4).

$$E(z) = E_1\left[1 - e_0\lambda(z)\right] \tag{1}$$

$$G(z) = \frac{E(z)}{2[1+\nu(z)]} \tag{2}$$

$$\rho(z) = \rho_1\left[1 - e_m\lambda(z)\right] \tag{3}$$

$$\alpha(z) = \alpha_1\left[1 - e_m\lambda(z)\right] \tag{4}$$

where

$$\lambda(z) = \begin{cases} \cos(\frac{\pi z}{h}) & \text{non-uniform symmetric porosity distribution} \\ \cos(\frac{\pi z}{2h} + \frac{\pi}{4}) & \text{non-uniform asymmetric porosity distribution} \\ \lambda & \text{uniform distribution} \end{cases} \tag{5}$$

e_0 denotes the coefficient of porosity which is defined by

$$e_0 = 1 - \frac{E_2}{E_1} \tag{6}$$

where E_1 and E_2 denote the maximum and minimum Young's modulus of the non-uniformly distributed porous material, respectively [34]. e_m represents the mass density coefficient. By introducing the typical mechanical property of the open-cell metal foam [31], the relationship between e_0 and e_m can be expressed as

$$e_m = 1 - \sqrt{1 - e_0} \tag{7}$$

For a uniform porous distribution, the coefficient λ can be determined as

$$\lambda = \frac{1}{e_0} - \frac{1}{e_0}\left(\frac{2}{\pi}\sqrt{1-e_0} - \frac{2}{\pi} + 1\right)^2 \tag{8}$$

The relationship between the volume and weight fractions is given by

$$\frac{\Lambda_{GPL}}{\Lambda_{GPL} + \frac{\rho_{GPL}}{\rho_M} - \frac{\rho_{GPL}}{\rho_M}\Lambda_{GPL}} \times \int_{-h/2}^{h/2}\left[1 - e_m\lambda(z)\right]dz = \int_{-h/2}^{h/2} V_{GPL}\left[1 - e_m\lambda(z)\right]dz \tag{9}$$

where V_{GPL} and Λ_{GPL} denote the volume and weight fractions of the GPL nanofillers, respectively.

According to the Halpin-Tsai micromechanics model [59–61], the elastic modulus of the porous core can be obtained as

$$E_1 = \frac{3}{8}\left(\frac{1 + \xi_L^{GPL}\eta_L^{GPL}V_{GPL}}{1 - \eta_L^{GPL}V_{GPL}}\right)E_M + \frac{5}{8}\left(\frac{1 + \xi_W^{GPL}\eta_W^{GPL}V_{GPL}}{1 - \eta_W^{GPL}V_{GPL}}\right)E_M \tag{10}$$

in which

$$\xi_L^{GPL} = \frac{2l_{GPL}}{t_{GPL}} \tag{11}$$

$$\xi_W^{GPL} = \frac{2w_{GPL}}{t_{GPL}} \tag{12}$$

$$\eta_L^{GPL} = \frac{(E_{GPL}/E_M) - 1}{(E_{GPL}/E_M) + \xi_L^{GPL}} \tag{13}$$

$$\eta_W^{GPL} = \frac{(E_{GPL}/E_M) - 1}{(E_{GPL}/E_M) + \xi_W^{GPL}} \tag{14}$$

where l_{GPL}, w_{GPL} and t_{GPL} represent the average length, width and thickness of the GPLs, respectively.

By applying the rule of mixture, the mass density ρ_1, the Poisson's ratio ν_1 and the thermal expansion coefficient α_1 of the GPL reinforced metal porous core can be calculated as

$$\rho_1 = \rho_{GPL}V_{GPL} + \rho_M V_M \tag{15}$$

$$\nu_1 = \nu_{GPL}V_{GPL} + \nu_M V_M \tag{16}$$

$$\alpha_1 = \frac{V_{GPL}E_{GPL}\alpha_{GPL} + V_M E_M \alpha_M}{V_{GPL}E_{GPL} + V_M E_M} \tag{17}$$

where ρ_{GPL}, ρ_M, ν_{GPL} and ν_M denote the densities of the GPLs and metal matrix, and the Poisson's ratios of the GPL and metal matrix, respectively. V_M represents the volume fraction of the matrix, which is related to the volume fraction of the GPLs as:

$$V_M = 1 - V_{GPL} \tag{18}$$

3. The fundamental formulations

From the classical laminated plate theory, the Von Kármán strain-displacement relationship bears the form

$$\begin{pmatrix}\varepsilon_x\\ \varepsilon_y\\ \gamma_{xy}\end{pmatrix} = \begin{pmatrix}\varepsilon_x^0\\ \varepsilon_y^0\\ \gamma_{xy}^0\end{pmatrix} + z\begin{pmatrix}\varepsilon_x^1\\ \varepsilon_y^1\\ \gamma_{xy}^1\end{pmatrix} \tag{19}$$

where

$$\left\{\varepsilon^0\right\} = \begin{Bmatrix}\varepsilon_x^{(0)}\\ \varepsilon_y^{(0)}\\ \gamma_{xy}^{(0)}\end{Bmatrix} = \begin{Bmatrix}\frac{\partial u}{\partial x} + \frac{1}{2}\left(\frac{\partial w}{\partial x}\right)^2\\ \frac{\partial v}{\partial y} + \frac{1}{2}\left(\frac{\partial w}{\partial y}\right)^2\\ \frac{\partial u}{\partial y} + \frac{\partial v}{\partial x} + \frac{\partial w}{\partial x}\frac{\partial w}{\partial y}\end{Bmatrix} \tag{20}$$

$$\left\{\varepsilon^1\right\} = \begin{Bmatrix}\varepsilon_x^1\\ \varepsilon_y^1\\ \gamma_{xy}^1\end{Bmatrix} = \begin{Bmatrix}-\frac{\partial^2 w}{\partial x^2}\\ -\frac{\partial^2 w}{\partial y^2}\\ -2\frac{\partial^2 w}{\partial x \partial y}\end{Bmatrix} \tag{21}$$

where u and v represent the displacement components along the x- and y-directions, respectively.

Based on the Hooke's law, the stress-strain relationships of the face layer and the porous core of the GPL-SFGP plate under a uniform thermal environment can be defined as

$$\begin{Bmatrix}\sigma_x\\ \sigma_y\\ \sigma_{xy}\end{Bmatrix}_f = \begin{bmatrix}Q_{11} & Q_{12} & 0\\ Q_{12} & Q_{22} & 0\\ 0 & 0 & Q_{66}\end{bmatrix}_f \begin{Bmatrix}(\varepsilon_x)_f - \varepsilon_x^T\\ (\varepsilon_y)_f - \varepsilon_y^T\\ (\gamma_{xy})_f\end{Bmatrix} \quad \text{and}$$

$$\begin{Bmatrix}\sigma_x\\ \sigma_y\\ \sigma_{xy}\end{Bmatrix}_c = \begin{bmatrix}Q_{11} & Q_{12} & 0\\ Q_{12} & Q_{22} & 0\\ 0 & 0 & Q_{66}\end{bmatrix}_c \begin{Bmatrix}(\varepsilon_x)_c - \varepsilon_x^T\\ (\varepsilon_y)_c - \varepsilon_y^T\\ (\gamma_{xy})_c\end{Bmatrix} \tag{22}$$

respectively. Moreover, the thermal strains are defined by

$$\begin{cases}\varepsilon_x^T = \alpha_x \Delta T(x, y, z, t)\\ \varepsilon_y^T = \alpha_y \Delta T(x, y, z, t)\end{cases} \tag{23}$$

where α_x and α_y are the thermal expansion coefficients along the x- and y-directions, respectively. The subscripts f and c denote the face layers and porous core layer, respectively. The coefficients Q_{ij} ($i,j = 1, 2, 6$) for the face layers and the porous core are given by

$$\begin{cases}(Q_{11})_f = \frac{E_f}{1-\nu_f^2}\\ (Q_{12})_f = \frac{\nu_f E_f}{1-\nu_f^2}\\ (Q_{22})_f = \frac{E_f}{1-\nu_f^2}\\ (Q_{66})_f = \frac{E_f}{2(1+\nu_f)}\end{cases} \tag{24}$$

$$\begin{cases}(Q_{11})_c = \frac{E(z)}{1-\nu(z)^2}\\ (Q_{12})_c = \frac{\nu(z)E(z)}{1-\nu(z)^2}\\ (Q_{22})_c = \frac{E(z)}{1-\nu(z)^2}\\ (Q_{66})_c = \frac{E(z)}{2[1+\nu(z)]}\end{cases} \tag{25}$$

where E_f and ν_f represent the Young's modulus and Poisson's ratios of the face layer, respectively.

The in-plane force and the moment resultants of the GPL-SFGP plate are calculated by

$$\begin{cases}N_i = \int_{\frac{h_c}{2}}^{h_f + \frac{h_c}{2}} (\sigma_i)_f dz + \int_{-\frac{h_c}{2}}^{\frac{h_c}{2}} (\sigma_i)_c dz + \int_{-(h_f + \frac{h_c}{2})}^{-\frac{h_c}{2}} (\sigma_i)_f dz\\ M_i = \int_{\frac{h_c}{2}}^{h_f + \frac{h_c}{2}} (\sigma_i \cdot z)_f dz + \int_{-\frac{h_c}{2}}^{\frac{h_c}{2}} (\sigma_i \cdot z)_c dz + \int_{-(h_f + \frac{h_c}{2})}^{-\frac{h_c}{2}} (\sigma_i \cdot z)_f dz\end{cases} \quad i = x, y, xy \tag{26}$$

Substituting Eqs. (19)–(25) into Eq. (26), the force and the moment resultants can be formulated as

$$\begin{bmatrix} N_x \\ N_y \\ N_{xy} \\ M_x \\ M_y \\ M_{xy} \end{bmatrix} = \begin{bmatrix} A_{11} & A_{12} & 0 & B_{11} & B_{12} & 0 \\ A_{12} & A_{22} & 0 & B_{12} & B_{22} & 0 \\ 0 & 0 & A_{66} & 0 & 0 & B_{66} \\ B_{11} & B_{12} & 0 & D_{11} & D_{12} & 0 \\ B_{12} & B_{22} & 0 & D_{12} & D_{22} & 0 \\ 0 & 0 & B_{66} & 0 & 0 & D_{66} \end{bmatrix} \begin{bmatrix} \varepsilon_x^0 - \varepsilon_x^T \\ \varepsilon_y^0 - \varepsilon_y^T \\ \gamma_{xy}^0 \\ \varepsilon_x^1 \\ \varepsilon_y^1 \\ \gamma_{xy}^1 \end{bmatrix} \tag{27}$$

where

$$\begin{aligned} &\{A_{ij}, B_{ij}, D_{ij}\} \\ &= \int_{\frac{h_c}{2}}^{h_f+\frac{h_c}{2}} (Q_{ij})_f \{1, z, z^2\} dz + \int_{-\frac{h_c}{2}}^{\frac{h_c}{2}} (Q_{ij})_c \{1, z, z^2\} dz \\ &\quad + \int_{-(h_f+\frac{h_c}{2})}^{-\frac{h_c}{2}} (Q_{ij})_f \{1, z, z^2\} dz \\ &\quad i, j = 1, 2, 6 \end{aligned} \tag{28}$$

From the classical plate theory, the nonlinear equilibrium equation of the GPL-SFGP plate resting on the Winkler–Pasternak elastic foundation with the consideration of damping effects can be formulated as

$$\frac{\partial N_x}{\partial x} + \frac{\partial N_{yx}}{\partial y} = \rho h \frac{\partial^2 u}{\partial t^2} + C_d \rho h \frac{\partial u}{\partial t} \tag{29}$$

$$\frac{\partial N_{xy}}{\partial x} + \frac{\partial N_y}{\partial y} = \rho h \frac{\partial^2 v}{\partial t^2} + C_d \rho h \frac{\partial v}{\partial t} \tag{30}$$

$$\begin{aligned} &\frac{\partial^2 M_x}{\partial x^2} + 2\frac{\partial^2 M_{xy}}{\partial x \partial y} + \frac{\partial^2 M_y}{\partial y^2} + N_x \frac{\partial^2 w}{\partial x^2} + 2N_{xy} \frac{\partial^2 w}{\partial x \partial y} \\ &\quad + N_y \frac{\partial^2 w}{\partial y^2} + q - k_w w + k_p \left(\frac{\partial^2 w}{\partial x^2} + \frac{\partial^2 w}{\partial y^2} \right) = \rho h \frac{\partial^2 w}{\partial t^2} + C_d \rho h \frac{\partial \omega}{\partial t} \end{aligned} \tag{31}$$

where C_d represents the viscous damping coefficient; k_w denotes the Winkler foundation modulus and k_p denotes the shear layer foundation stiffness of the Pasternak model; q represents the uniformly distributed external pressure applied on the plate. In this study, it is assumed that the flexural motion dominates the overall structural deformation, i.e., $u \ll w$, and $v \ll w$, so $\frac{\partial^2 u}{\partial t^2}$, $\frac{\partial u}{\partial t}$, $\frac{\partial^2 v}{\partial t^2}$, and $\frac{\partial v}{\partial t}$ are negligible. According to Eqs. (27)–(31), the stress function $f(x, y)$ can be defined by

$$N_x = \frac{\partial^2 f}{\partial x^2}, N_y = \frac{\partial^2 f}{\partial y^2}, N_{xy} = -\frac{\partial^2 f}{\partial x \partial y} \tag{32}$$

By considering the initial imperfection, the geometric compatibility equation for the GPL-SFGP plate can be formulated as

$$\begin{aligned} &\frac{\partial^2 \varepsilon_x^0}{\partial y^2} + \frac{\partial^2 \varepsilon_y^0}{\partial x^2} - \frac{\partial^2 \gamma_{xy}^0}{\partial x \partial y} \\ &= \left(\frac{\partial^2 w}{\partial x \partial y} \right)^2 - \frac{\partial^2 w}{\partial x^2} \frac{\partial^2 w}{\partial y^2} + 2\frac{\partial^2 w}{\partial x \partial y} \frac{\partial^2 w^*}{\partial x \partial y} - \frac{\partial^2 w}{\partial x^2} \frac{\partial^2 w^*}{\partial y^2} - \frac{\partial^2 w}{\partial y^2} \frac{\partial^2 w^*}{\partial x^2} \end{aligned} \tag{33}$$

where $w^*(x, y)$ is a function which represents the initial imperfection of the plate.

From Eq. (27), the membrane strains can be rewritten as

$$\begin{cases} \varepsilon_x^0 = A_{11}^* N_x + A_{12}^* N_y + A_{13}^* \varepsilon_x^1 + A_{14}^* \varepsilon_y^1 + \varepsilon_x^T \\ \varepsilon_y^0 = A_{12}^* N_x + A_{22}^* N_y + A_{23}^* \varepsilon_x^1 + A_{24}^* \varepsilon_y^1 + \varepsilon_y^T \\ \gamma_{xy}^0 = A_{31}^* N_{xy} + A_{32}^* \gamma_{xy}^1 \end{cases} \tag{34}$$

with

$$A_{11}^* = \frac{A_{22}}{A_{11}A_{22} - A_{12}^2} \tag{35}$$

$$A_{12}^* = -\frac{A_{12}}{A_{11}A_{22} - A_{12}^2} \tag{36}$$

$$A_{13}^* = \frac{A_{12}B_{12} - A_{22}B_{11}}{A_{11}A_{22} - A_{12}^2} \tag{37}$$

$$A_{14}^* = \frac{A_{12}B_{22} - A_{22}B_{12}}{A_{11}A_{22} - A_{12}^2} \tag{38}$$

$$A_{22}^* = \frac{A_{11}}{A_{11}A_{22} - A_{12}^2} \tag{39}$$

$$A_{23}^* = \frac{A_{12}B_{11} - A_{11}B_{12}}{A_{11}A_{22} - A_{12}^2} \tag{40}$$

$$A_{24}^* = \frac{A_{12}B_{12} - A_{11}B_{22}}{A_{11}A_{22} - A_{12}^2} \tag{41}$$

$$A_{31}^* = \frac{1}{A_{66}} \tag{42}$$

$$A_{32}^* = -\frac{B_{66}}{A_{66}} \tag{43}$$

By substituting Eq. (34) into Eq. (33), for the environment with uniform temperature variations, the nonlinear compatibility equation of the GPL-SFGP plate with initial imperfection can be obtained as:

$$\begin{aligned} &A_{22}^* \frac{\partial^4 f}{\partial x^4} + A_{11}^* \frac{\partial^4 f}{\partial y^4} + \left(2A_{12}^* + A_{31}^*\right) \frac{\partial^4 f}{\partial x^2 \partial y^2} \\ &\quad - A_{23}^* \frac{\partial^4 w}{\partial x^4} - A_{14}^* \frac{\partial^4 w}{\partial y^4} + \left(2A_{32}^* - A_{13}^* - A_{24}^*\right) \frac{\partial^4 w}{\partial x^2 \partial y^2} \\ &= \left(\frac{\partial^2 w}{\partial x \partial y} \right)^2 - \frac{\partial^2 w}{\partial x^2} \frac{\partial^2 w}{\partial y^2} + 2\frac{\partial^2 w}{\partial x \partial y} \frac{\partial^2 w^*}{\partial x \partial y} - \frac{\partial^2 w}{\partial x^2} \frac{\partial^2 w^*}{\partial y^2} - \frac{\partial^2 w}{\partial y^2} \frac{\partial^2 w^*}{\partial x^2} \end{aligned} \tag{44}$$

By substituting Eq. (34) into Eq. (27), and then substitute the resultant into Eq. (31), the equation of motion of the GPL-SFGP plate can be reformulated as:

$$\begin{aligned} &T_{11} \frac{\partial^4 f}{\partial x^4} + T_{12} \frac{\partial^4 f}{\partial y^4} + T_{13} \frac{\partial^4 f}{\partial x^2 \partial y^2} + T_{14} \frac{\partial^4 w}{\partial x^4} \\ &\quad + T_{15} \frac{\partial^4 w}{\partial y^4} + T_{16} \frac{\partial^4 w}{\partial x^2 \partial y^2} + \frac{\partial^2 f}{\partial y^2} \frac{\partial^2 w}{\partial x^2} - 2\frac{\partial^2 f}{\partial x \partial y} \frac{\partial^2 w}{\partial x \partial y} \\ &\quad + \frac{\partial^2 f}{\partial x^2} \frac{\partial^2 w}{\partial y^2} + q - k_w w + k_p \left(\frac{\partial^2 w}{\partial x^2} + \frac{\partial^2 w}{\partial y^2} \right) = \rho h \frac{\partial^2 w}{\partial t^2} + C_d \rho h \frac{\partial w}{\partial t} \end{aligned} \tag{45}$$

with

$$\begin{aligned} T_{11} &= B_{11}A_{12}^* + B_{12}A_{22}^* \\ T_{12} &= B_{12}A_{11}^* + B_{22}A_{12}^* \\ T_{13} &= B_{11}A_{11}^* + 2B_{12}A_{12}^* - 2B_{66}A_{31}^* + B_{22}A_{22}^* \\ T_{14} &= -\left(B_{11}A_{13}^* + B_{12}A_{23}^* + D_{11}\right) \\ T_{15} &= -\left(B_{12}A_{14}^* + B_{22}A_{24}^* + D_{22}\right) \\ T_{16} &= -\left(B_{11}A_{14}^* + B_{12}A_{24}^* + 2D_{12} + 4(B_{66}A_{32}^* + D_{66}) + B_{12}A_{13}^* + B_{22}A_{23}^*\right) \end{aligned} \tag{46}$$

Taking the initial imperfection into consideration, for a GPL-SFGP plate resting on the Winkler–Pasternak elastic foundation, the equation of motion can be explicitly formulated as:

$$\begin{aligned} &T_{11} \frac{\partial^4 f}{\partial x^4} + T_{12} \frac{\partial^4 f}{\partial y^4} + T_{13} \frac{\partial^4 f}{\partial x^2 \partial y^2} + T_{14} \left(\frac{\partial^4 w}{\partial x^4} + \frac{\partial^4 w^*}{\partial x^4} \right) \\ &\quad + T_{15} \left(\frac{\partial^4 w}{\partial y^4} + \frac{\partial^4 w^*}{\partial y^4} \right) + T_{16} \left(\frac{\partial^4 w}{\partial x^2 \partial y^2} + \frac{\partial^4 w^*}{\partial x^2 \partial y^2} \right) + \frac{\partial^2 f}{\partial y^2} \left(\frac{\partial^2 w}{\partial x^2} + \frac{\partial^2 w^*}{\partial x^2} \right) \\ &\quad - 2\frac{\partial^2 f}{\partial x \partial y} \left(\frac{\partial^2 w}{\partial x \partial y} + \frac{\partial^2 w^*}{\partial x \partial y} \right) + \frac{\partial^2 f}{\partial x^2} \left(\frac{\partial^2 w}{\partial y^2} + \frac{\partial^2 w^*}{\partial y^2} \right) + q - k_w w \\ &\quad + k_p \left(\frac{\partial^2 w}{\partial x^2} + \frac{\partial^2 w}{\partial y^2} \right) = \rho h \frac{\partial^2 w}{\partial t^2} + C_d \rho h \frac{\partial w}{\partial t} \end{aligned} \tag{47}$$

4. Nonlinear dynamic analysis

In this study, the four edges of the plate are assumed to be simply supported and remain straight after buckling. Thus, such adoption of the boundary conditions implies that

$$\left.\begin{matrix} w = u = M_x = 0 \\ N_x = N_{x0} \end{matrix}\right\} x = 0, a \tag{48}$$

$$\left.\begin{matrix} w = v = M_y = 0 \\ N_y = 0 \end{matrix}\right\} y = 0, b \tag{49}$$

where $N_{x0} = -p(t)h$ is the compressive load along the x-direction.

The solution of the plate deflection w, which satisfies the boundary conditions, is assumed to be [62]:

$$w(x, y, t) = W(t)\sin\left(\frac{m\pi x}{a}\right)\sin\left(\frac{n\pi y}{b}\right) \tag{50}$$

where $W(t)$ represents the time-dependent function of w; m and n are odd integers that indicate the number of half waves in x- and y-directions, respectively.

The initial imperfection, $w^*(x, y)$, is presumed to have the same format of $w(x, y, t)$,

$$w^*(x, y) = W_0\sin\left(\frac{m\pi x}{a}\right)\sin\left(\frac{n\pi y}{b}\right) \tag{51}$$

where W_0 denotes the amplitude.

The solution of the stress function, which satisfies the boundary conditions, is assumed to be:

$$\begin{aligned} f(x, y, t) = {} & H_1\cos\left(\frac{2m\pi x}{a}\right) + H_2\cos\left(\frac{2n\pi y}{b}\right) \\ & + H_3\sin\left(\frac{m\pi x}{a}\right)\sin\left(\frac{n\pi y}{b}\right) + \frac{1}{2}N_{x0}y^2 \end{aligned} \tag{52}$$

where

$$\begin{aligned} H_1 &= \frac{\left(W^2 + 2WW_0\right)\left(\frac{n\pi}{b}\right)^2}{32A_{22}^*\left(\frac{m\pi}{a}\right)^2} \\ H_2 &= \frac{\left(W^2 + 2WW_0\right)\left(\frac{m\pi}{a}\right)^2}{32A_{11}^*\left(\frac{n\pi}{b}\right)^2} \\ H_3 &= \frac{A_{14}^*\left(\frac{n\pi}{b}\right)^4 + A_{23}^*\left(\frac{m\pi}{a}\right)^4 - \left(2A_{32}^* - A_{13}^* - A_{24}^*\right)\left(\frac{m\pi}{a}\right)^2\left(\frac{n\pi}{b}\right)^2}{A_{11}^*\left(\frac{n\pi}{b}\right)^4 + A_{22}^*\left(\frac{m\pi}{a}\right)^4 + \left(2A_{12}^* + A_{31}^*\right)\left(\frac{m\pi}{a}\right)^2\left(\frac{n\pi}{b}\right)^2}W \end{aligned} \tag{53}$$

Substituting Eqs. (50)–(53) into Eq. (47), and with the assumption of $\alpha = m\pi/a$, $\beta = n\pi/b$, the equaiton of motion of the plate can be reformulated as:

$$\begin{aligned} & T_{11}\left[16H_1\alpha^4\cos(2\alpha x) + H_3\alpha^4\sin(\alpha x)\sin(\beta y)\right] \\ & + T_{12}\left[16H_2\beta^4\cos(2\beta y) + H_3\beta^4\sin(\alpha x)\sin(\beta y)\right] \\ & + T_{13}\left[\alpha^2\beta^2 H_3\sin(\alpha x)\sin(\beta y)\right] \\ & + T_{14}\left[\alpha^4\sin(\alpha x)\sin(\beta y)\right](W + W_0) + T_{15}\left[\beta^4\sin(\alpha x)\sin(\beta y)\right](W + W_0) \\ & + T_{16}\left[\alpha^2\beta^2\sin(\alpha x)\sin(\beta y)\right](W + W_0) \\ & + \left[4H_2\beta^2\cos(2\beta y) + H_3\beta^2\sin(\alpha x)\sin(\beta y) - N_{x0}\right] \\ & \quad \times\left[\alpha^2\sin(\alpha x)\sin(\beta y)(W + W_0)\right] \\ & - 2\left[H_3\alpha\beta\cos(\alpha x)\cos(\beta y)\right]\left[\alpha\beta\cos(\alpha x)\cos(\beta y)(W + W_0)\right] \\ & + \left[4H_1\alpha^2\cos(2\alpha x) + H_3\alpha^2\sin(\alpha x)\sin(\beta y)\right]\left[\beta^2\sin(\alpha x)\sin(\beta y)(W + W_0)\right] \\ & + q - k_w\sin(\alpha x)\sin(\beta y)W - k_p\left[\left(\alpha^2 + \beta^2\right)\sin(\alpha x)\sin(\beta y)W\right] \\ = {} & \rho h\frac{\partial^2 W}{\partial t^2}\sin(\alpha x)\sin(\beta y) + C_d\rho h\frac{\partial W}{\partial t}\sin(\alpha x)\sin(\beta y) \end{aligned} \tag{54}$$

By adopting the Galerkin method, $\sin(m\pi x/a)\sin(n\pi y/b)$ is multiplied with each term in Eq. (54), and then integrated over the middle surface of the GPL-SFGP plate. Consequently, the resultant equation can be expressed as

$$\begin{aligned} & P_1(W + 2W_0)W + P_2W + P_3(W + W_0) + P_4(W + W_0)(W + 2W_0)W \\ & + P_5(W + W_0)W + P_6q - N_{x0}\alpha^2(W + W_0) - \left[k_w + k_p\cdot\left(\alpha^2 + \beta^2\right)\right]W \\ = {} & \rho h\frac{\partial^2 W}{\partial t^2} + C_d\rho h\frac{\partial W}{\partial t} \end{aligned} \tag{55}$$

where

$$\begin{aligned} P_1 &= -\left(\frac{T_{12}}{A_{11}^*} + \frac{T_{11}}{A_{22}^*}\right)\cdot\frac{8}{3}\frac{\alpha\beta}{ab} \\ P_2 &= \left(T_{11}\alpha^4 + T_{12}\beta^4 + T_{13}\alpha^2\beta^2\right)\cdot\left[\frac{A_{14}^*\beta^4 + A_{23}^*\alpha^4 - \left(2A_{32}^* - A_{13}^* - A_{24}^*\right)\alpha^2\beta^2}{A_{11}^*\beta^4 + A_{22}^*\alpha^4 + \left(2A_{12}^* + A_{31}^*\right)\alpha^2\beta^2}\right] \\ P_3 &= \left(T_{14}\alpha^4 + T_{15}\beta^4 + T_{16}\alpha^2\beta^2\right) \\ P_4 &= -\left(\frac{\alpha^4}{16A_{11}^*} + \frac{\beta^4}{16A_{22}^*}\right) \\ P_5 &= \frac{32\alpha\beta}{3ab}\cdot\frac{A_{14}^*\beta^4 + A_{23}^*\alpha^4 - \left(2A_{32}^* - A_{13}^* - A_{24}^*\right)\alpha^2\beta^2}{A_{11}^*\beta^4 + A_{22}^*\alpha^4 + \left(2A_{12}^* + A_{31}^*\right)\alpha^2\beta^2} \\ P_6 &= \frac{4}{\alpha\beta}\frac{4}{ab} \end{aligned} \tag{56}$$

It is assumed that the plate is subjected to a uniformly distributed external pressure $q = Q\sin\Omega t$, where Q and Ω denote the amplitude and frequency of the excitation, respectively. Consequently, Eq. (55) becomes

$$\begin{aligned} & P_1\left(W + 2W_0\right)W + P_2W + P_3(W + W_0) + P_4(W + W_0)(W + 2W_0)W \\ & + P_5(W + W_0)W + P_6Q\sin(\Omega t) + p(t)\alpha^2h(W + W_0) - \left[k_w + k_p(\alpha^2 + \beta^2)\right]W \\ = {} & \rho h\frac{\partial^2 W}{\partial t^2} + C_d\rho h\frac{\partial W}{\partial t} \end{aligned} \tag{57}$$

According to Eqs. (20) and (34), with the consideration of the initial imperfection of the plate, the expression of the strain along the x-axial can be obtained as

$$\begin{aligned} \frac{\partial u}{\partial x} = {} & -4\beta^2A_{11}^*H_2\cos(2\beta y) - 4\alpha^2A_{12}^*H_1\cos(2\alpha x) - A_{11}^*p(t)h \\ & - \left(A_{11}^*\beta^2 + A_{12}^*\alpha^2\right)H_3\sin(\alpha x)\sin(\beta y) + \left(A_{13}^*\alpha^2 + A_{14}^*\beta^2\right)W\sin(\alpha x)\sin(\beta y) \\ & - \alpha^2\left(\frac{1}{2}W + W_0\right)W\cos^2(\alpha x)\cos^2(\beta y) + \varepsilon_x^T \end{aligned} \tag{58}$$

To apply a dynamic compressive load on the longitudinal direction of the plate, a constant displacement rate v is exerted on the edge of the plate along the x-axis. Thus, the relative edge displacement of the plate along the x- direction is given as

$$U = \int_0^b\int_0^a\frac{\partial u}{\partial x}dxdy = -\mathrm{v}t \tag{59}$$

Substituting Eq. (58) into Eq. (59) produces an average compressive stress as

$$\begin{aligned} p(t) = {} & -\frac{\left(A_{11}^*\beta^2 + A_{12}^*\alpha^2\right)}{A_{11}^*abh}\frac{4}{\alpha\beta}H_3 + \frac{\varepsilon_x^T}{A_{11}^*h} + \frac{\left(A_{13}^*\alpha^2 + A_{14}^*\beta^2\right)}{A_{11}^*abh}\frac{4}{\alpha\beta}W \\ & - \frac{\left(W + 2W_0\right)W\alpha^2}{8A_{11}^*h} + \frac{\mathrm{v}t}{A_{11}^*abh} \end{aligned} \tag{60}$$

4.1. Nonlinear dynamic response analysis

By neglecting the damping effect of an unloaded perfect plate, Eq. (57) can be reduced into

$$\frac{\partial^2 W}{\partial t^2} - \frac{\left[P_2 + P_3 - k_w - k_p\left(\alpha^2 + \beta^2\right)\right]}{\rho h}W - \frac{\left(P_1 + P_5\right)}{\rho h}W^2 - \frac{P_4}{\rho h}W^3 = 0 \tag{61}$$

Without the consideration of the nonlinearity, the natural frequency of the perfect GPL-SFGP plate can be obtained from the coefficient of W in Eq. (61). That is,

$$\omega_{\mathrm{mn}} = \sqrt{-\frac{P_2 + P_3 - \left[k_w + k_p\left(\alpha^2 + \beta^2\right)\right]}{\rho h}} \tag{62}$$

Table 1
The adopted material properties.

	Young's modulus (GPa)	Density (kg/m^3)	Poisson's ratio	Thermal expansion coefficient (K^{-1})
Aluminum	68.3	2689.8	0.34	23e–6
GPL	1010	1062.5	0.186	5e–6

By considering the harmonic vibration, the solution of $W(t)$ can be adopted as:

$$W(t) = A\sin(\Omega t) \tag{63}$$

Assuming the compressive loading rate v = 0, for the nonlinear vibration of an initially perfect GPL-SFGP plate with the consideration of damping effects, Eq. (57) bears the form

$$\frac{\partial^2 W}{\partial t^2} + C_d\frac{\partial W}{\partial t} + {\omega_{mn}}^2 W - \frac{\varepsilon_x^T\alpha^2}{A_{11}^*\rho h}W - \frac{h\alpha^2\varphi + P_1 + P_5}{\rho h}W^2 - \frac{P_4 + h\alpha^2\psi}{\rho h}W^3 - \frac{P_6}{\rho h}Q sin\Omega t = 0 \tag{64}$$

where

$$\varphi = -\frac{4}{\alpha\beta}\frac{\left(A_{11}^*\beta^2 + A_{12}^*\alpha^2\right)}{A_{11}^* abh}\frac{A_{14}^*\beta^4 + A_{23}^*\alpha^4 - \left(2A_{32}^* - A_{13}^* - A_{24}^*\right)\alpha^2\beta^2}{A_{11}^*\beta^4 + A_{22}^*\alpha^4 + \left(2A_{12}^* + A_{31}^*\right)\alpha^2\beta^2} + \frac{4}{\alpha\beta}\frac{\left(A_{13}^*\alpha^2 + A_{14}^*\beta^2\right)}{A_{11}^* abh} \tag{65}$$

$$\psi = -\frac{\alpha^2}{8A_{11}^* h} \tag{66}$$

$$C_d = 2\omega_{mn}\zeta \tag{67}$$

where ζ is the damping ratio of the plate.

By applying the Galerkin procedure to the resultant formulation, which was obtained by substituting Eq. (63) into Eq. (64), the nonlinear vibration equation of the plate can be transformed into

$$\Omega^2 - \frac{2}{\pi}C_d\Omega - {\omega_{mn}}^2 + \frac{8A}{3\pi}\frac{h\alpha^2\varphi + P_1 + P_5}{\rho h} + \frac{3}{4}\frac{P_4 + h\alpha^2\psi}{\rho h}A^2 + \frac{\varepsilon_x^T\alpha^2}{A_{11}^*\rho h} + \frac{P_6}{\rho hA}Q = 0 \tag{68}$$

4.2. Dynamic buckling analysis

Considering an initially perfect GPL-SFGP plate, the corresponding linear static behavior can be obtained by omitting the uniformly distributed external pressure, the high-order term, the acceleration term and the velocity term from Eq. (57). That is,

$$P_2 + P_3 + p(t)h\alpha^2 - \left[k_w + k_p\left(\alpha^2 + \beta^2\right)\right] = 0 \tag{69}$$

Then the critical buckling load can be determined as

$$p_{st} = \frac{1}{h\alpha^2}\left[k_w + k_p\left(\alpha^2 + \beta^2\right) - P_2 - P_3\right] \tag{70}$$

By substituting Eq. (60) into Eq. (57), the equation describing the dynamic buckling behavior of the GPL-SFGP plate with initial imperfection is given as

$$\frac{P_1}{\rho h}(W + 2W_0)W + \frac{P_2}{\rho h}W + \frac{P_3}{\rho h}(W + W_0) + \frac{P_4}{\rho h}(W + W_0)(W + 2W_0)W + \frac{P_5}{\rho h}(W + W_0)W + \frac{P_6}{\rho h}Q\sin(\Omega t) - \frac{1}{\rho h}\left[k_w + k_p\left(\alpha^2 + \beta^2\right)\right]W + \frac{\alpha^2}{\rho}(W + W_0)[\varphi W + \frac{\varepsilon_x^T}{A_{11}^* h} + \psi(W + 2W_0)W + \frac{\mathrm{v}t}{A_{11}^* abh}] = \frac{\partial^2 W}{\partial t^2} + C_d\frac{\partial W}{\partial t} \tag{71}$$

By solving Eq. (71), the buckling load can be obtained from Eq. (60) accordingly.

5. Numerical results and discussions

The adopted material properties of the GPL-SFGP plate for all subsequent numerical investigations are presented in Table 1.

5.1. Validation analysis

Since there are not any available results for the GPL-SFGP plate under the currently concerned conditions, the proposed method is validated against the commercial Finite Element Method (FEM) package, ANSYS.

A uniformly distributed porous core reinforced by uniformly distributed GPL and orthotropic metal face layers are considered in the free vibration of the GPL-SFGP plate. The dimensions of the plate are $a = b = 1m$, $h = 0.005a$, $h_f = 0.1h$, $h_c = 0.8h$, $e_0 = 0.5$.For the GPLs, the parameters are selected as $l_{GPL} = 2.5\mu$m, $w_{GPL} = 1.5\mu$m, $t_{GPL} = 1.5$nm and $\Lambda_{GPL} = 1wt\%$.

By neglecting the effect of the elastic foundation, different modes of the natural frequency of the plate computed by presented method are compared with the results obtained from ANSYS. Since there is not a direct element type that exactly matching the GPL-SFGP plate in ANSYS, the SHELL 281 element has been adopted for the purpose of validation. In order to model the functionally graded porous material, the cross-section of the GPL-SFGP plate has been discretized into 200 layers and each layer with a constant material property. Furthermore, the GPL-SFGP plate has been meshed with an element length = 0.02 m. The numerical results on the natural frequencies of the GPL-SFGP plate through the two methods are reported in Table 2.

Table 2
Natural frequencies of the GPL-SFGP plate without considering Winkler–Pasternak elastic foundation.

Mode type (m, n)	Proposed method (rad/s)	ANSYS (rad/s)	Related error* (%)
(1,1)	160.6964	159.1782	0.9538
(1,3)	803.4820	795.7654	0.9697
(3,3)	1446.2676	1429.8645	1.1472
(3,5)	2731.8389	2699.7591	1.1882

$$\text{Related error} = \frac{\text{Presented value} - \text{ANSYS value}}{\text{ANSYS value}} \times 100\%$$

It can be observed from Table 2 that the natural frequencies of the plate obtained by the proposed method generally agree with the numerical results.

Furthermore, Table 3 demonstrates the influences of different Winkler–Pasternak elastic foundation parameters on the natural frequency of the plate. The values of the natural frequencies are increased

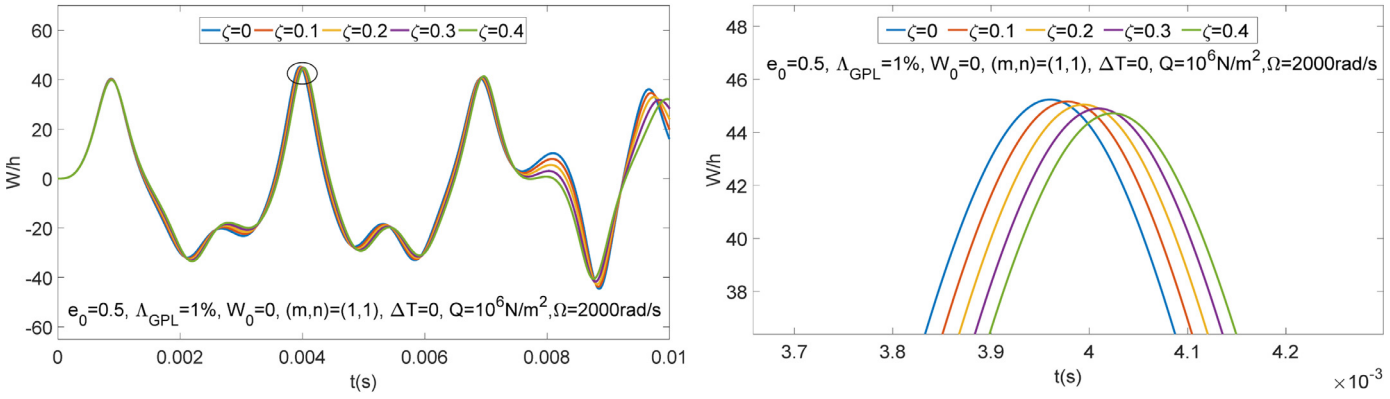

Fig. 3. (a) Effect of the damping ratio on the nonlinear dynamic response of the GPL-SFGP plate; (b) Zoomed-in view of (a).

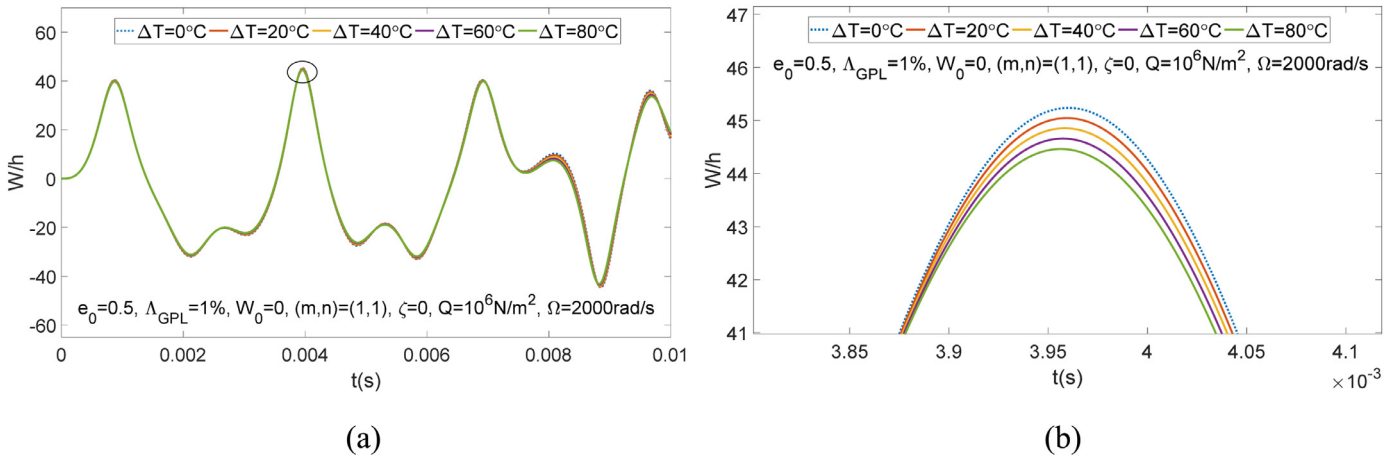

Fig. 4. (a) Influence of the temperature increment on the nonlinear dynamic response of the GPL-SFGP plate; (b) Zoomed-in view of (a).

Table 3
Effects of the Winkler–Pasternak foundation parameters on the natural frequencies of the GPL-SFGP plate.

k_w (N/m^2)	k_p (N/m)	(m, n)			
		(1,1)	(1,3)	(3,3)	(3,5)
0	500,000	539.172	1322.491	1918.327	2993.348
500,000	0	169.563	619.106	1100.251	2069.597
500,000	500,000	551.983	1327.766	1921.967	2995.682

with the enlargements of the elastic foundation parameters. It is noticed that k_p, which is the Pasternak shear layer foundation stiffness, has greater impact on the natural frequencies of the plate than k_w, which is the Winkler foundation mudulus.

5.2. Nonlinear dynamic responses

To explore the influences of the damping ratio, thermal variation, external excitation, elastic foundation, porosity, GPL weight fraction and GPL dimensions on the nonlinear dynamic responses of the GPL-SFGP plate, the fourth-order Runge–Kutta method is employed to solve Eq. (64). The initial conditions are assumed to be $W(0) = 0$, $dW(0)/dt = 0$. A negative value of the thermal expansion coefficient of the plate is adopted for the rising temperature from the basic temperature ($T = 300$K). The Winkler–Pasternak elastic foundation coefficients are $k_w = 1 \times 10^5$N/m^2, $k_p = 1 \times 10^3$N/m.

Fig. 3 shows the effect of damping ratio on the nonlinear dynamic response of the initially perfect GPL-SFGP plate. Five sets of damping ratios are considered with $\zeta = [0, 0.1, 0.2, 0.3, 0.4]$. To enhance the visualization on the difference between the five curves, a zoomed-in view of Fig. 3(a) is showed in Fig. 3(b). It is discovered that the nonlinear dynamic response of the plate decreases when the damping ratio is increased.

Fig. 4 illustrates the effect of thermal variation on the nonlinear dynamic response of the initially perfect GPL-SFGP plate. Fig. 4(b) is the zoom-in of Fig. 4(a). Five cases, namely ΔT= [0°C, 20°C, 40°C, 60°C, 80°C], are considered. It should be noticed that the increase of the magnitude of the temperature increment reduces the amplitude of vibration of the plate. One possible reason for such phenomenon is that the rise of temperature counteracts the effects of the oppositely applied compressive loading on the plate.

Fig. 5(a) and (b) demonstrate the impact of the magnitudes and the frequencies of the external excitation on the nonlinear dynamic response of the GPL-SFGP plate, respectively. For the same frequency of the excitation, the amplitude of the plate grows significantly with the increasing of magnitude of the external excitation, but the period of vibration almost remains the same. However, as shown in Fig. 5(b), the variation of the frequency of the external excitation influences both the periods and amplitudes of the nonlinear response of the plate.

Fig. 6 illustrates the impact of the Winkler–Pasternak foundation coefficients, k_w and k_p, on the nonlinear dynamic response of the GPL-SFGP plate. A zoomed-in view of Fig. 6(a) is presented in Fig. 6(b).

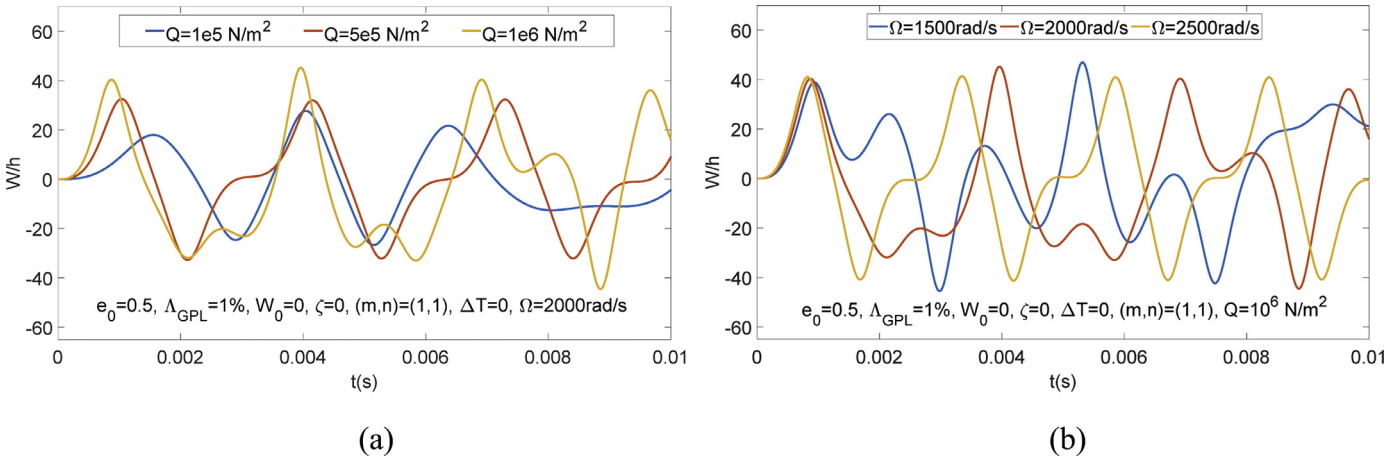

Fig. 5. Influence of (a) the magnitude and (b) the frequency of the external excitation on the nonlinear dynamic response of the GPL-SFGP plate.

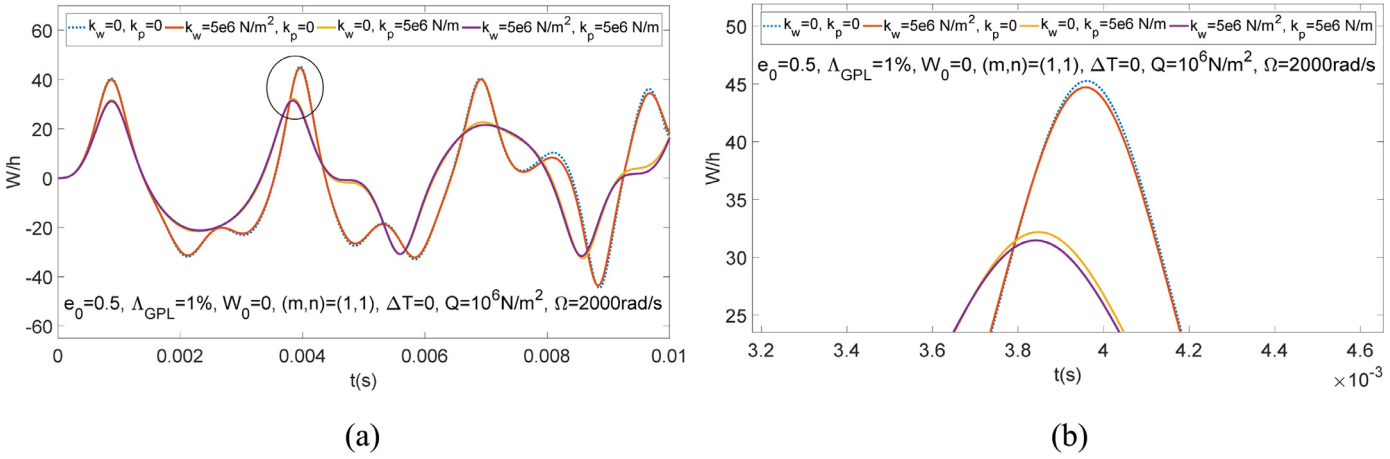

Fig. 6. (a) Influence of the Winkler–Pasternak foundation on the nonlinear dynamic response of the GPL-SFGP plate; (b) Zoomed-in view of (a).

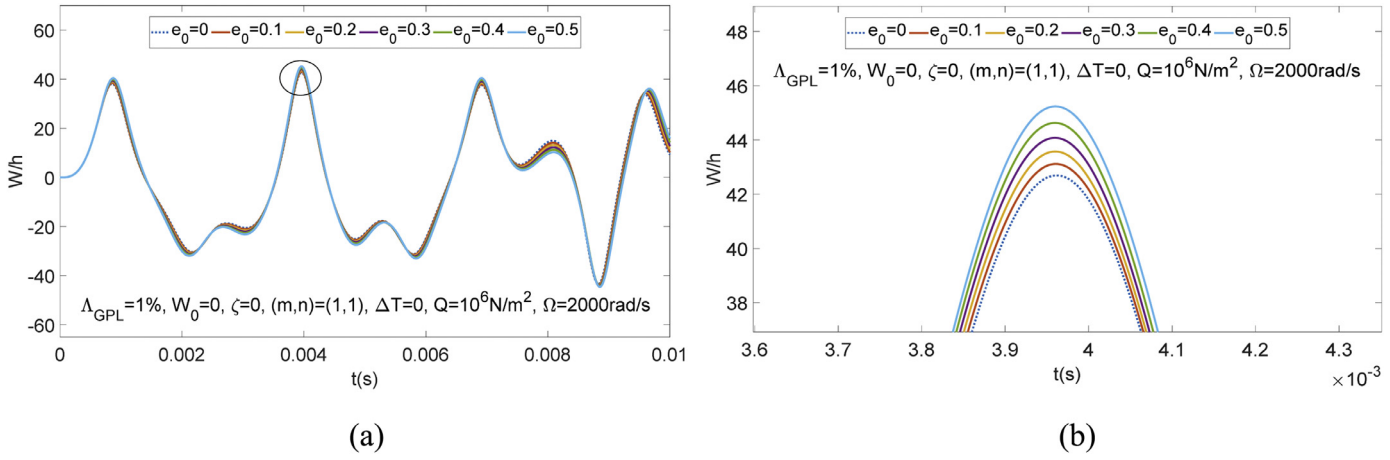

Fig. 7. (a) Influence of the porosity of the nonlinear dynamic response of the GPL-SFGP plate; (b) Zoomed-in view of Figure 7 (a).

From Fig. 6, it is demonstrated that the amplitudes of the nonlinear dynamic response of the plate reduce due to the existence of the elastic foundation. In addition, the benefit provided by the Pasternak shear layer foundation stiffness, k_p, is more prominent than the Winkler foundation modulus, k_w.

The nonlinear dynamic response of the GPL-SFGP plate with various porosities (i.e., $e_0 = [0, 0.1, 0.2, 0.3, 0.4, 0.5]$) are investigated and, the corresponding results are reported in Fig. 7. Fig. 7(b) is the zoom-in of Fig. 7(a). It is discovered that the amplitude of the transverse deflection of the GPL-SFGP plate increases with the rise of the porosity of the plate. The porosity of the plate is a key parameter which balances the weight

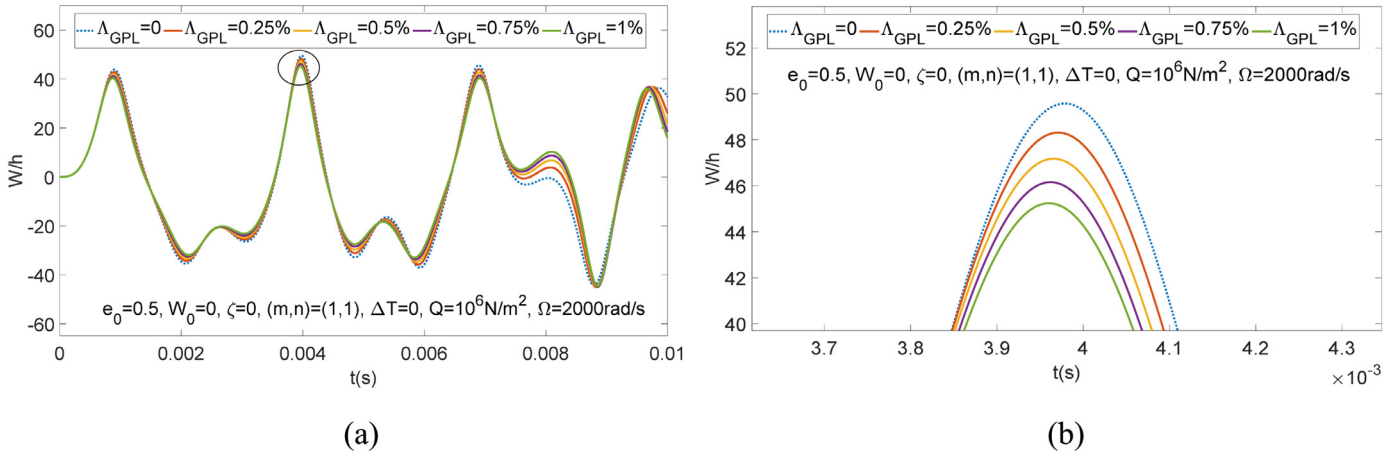

Fig. 8. (a) Influence of the GPL weight fraction on the nonlinear dynamic response of the GPL- SFGP plate; (b) Zoomed-in view of Figure 8 (a).

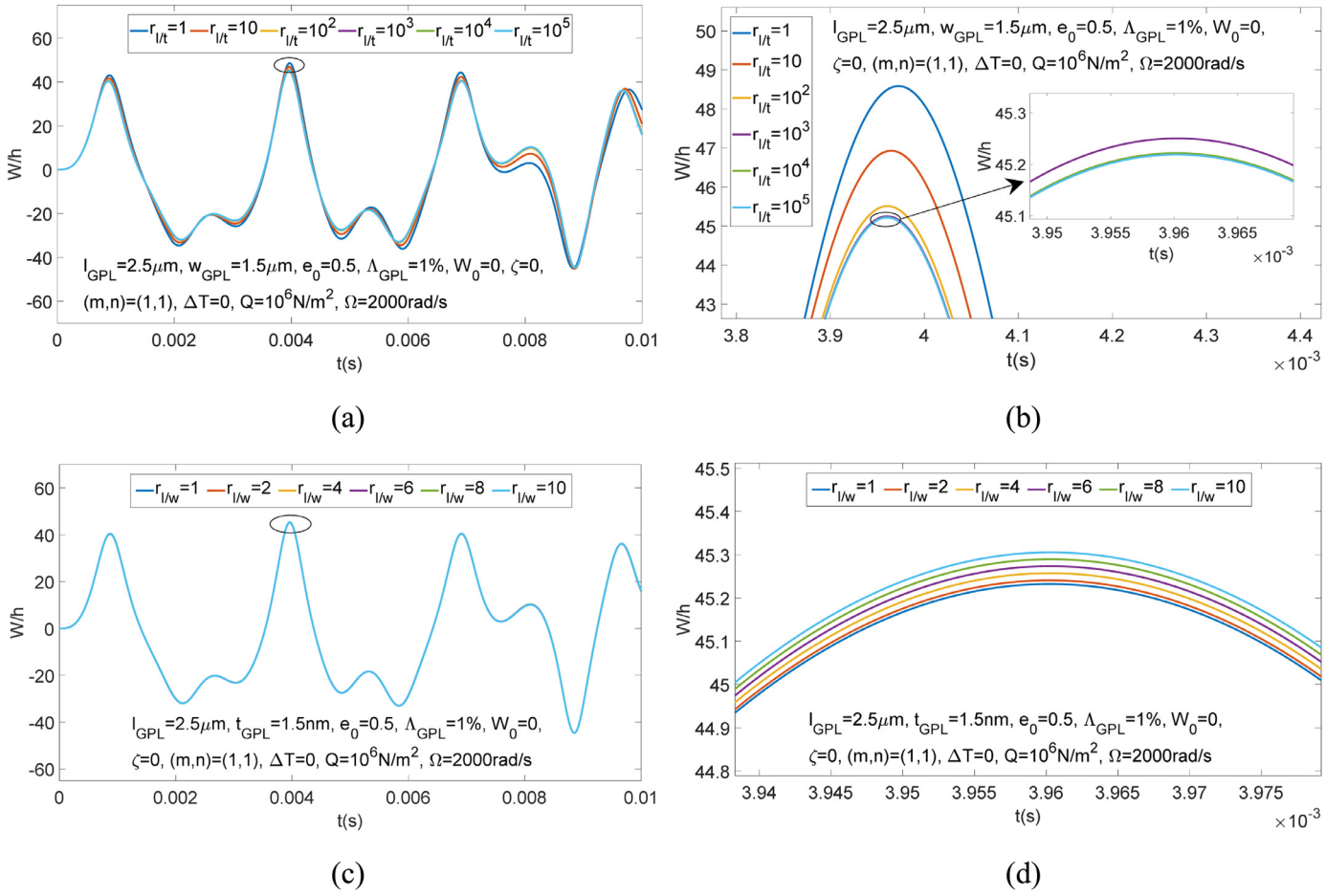

Fig. 9. (a) Influence of $r_{l/t}$ on the nonlinear dynamic response of the GPL- SFGP plate; (b) Zoomed-in view of Figure 9 (a); (c) Influence of $r_{l/w}$ on the nonlinear dynamic response of the GPL- SFGP plate; (d) Zoomed-in view of Figure 9 (c).

and stiffness of the plate. That is, increasing the porosity of the plate would reduce the capacity of itself against external excitation.

Fig. 8 illustrates the effect of various GPL weight fractions on the nonlinear dynamic response of the GPL-SFGP plate. Five different GPL weight fractions, which are from 0% to 1% with an increment of 0.25%, are considered. A zoomed-in view of Fig. 8(a) is presented in Fig. 8(b). Clearly, the addition of the GPL reduces the vibration of the GPL-SFGP plate due to the enhancement of the overall structural stiffness.

The effect of the dimension of the GPLs on the nonlinear dynamic response of the GPL- SFGP plate is indicated in Fig. 9. As clearly demonstrated in Fig. 9(a) and (b), for the same width of the GPLs, the increase of the length-to-thick ratio of the GPL (i.e., $r_{l/t} = l_{GPL}/t_{GPL}$) can effectively reduce the amplitude of the vibration. However, when the length-to-thick ratio is larger than 10^3, no further reduction of the vibration of the GPL-SFGP plate can be observed in Fig. 9(b). Therefore, $r_{l/t} = l_{GPL}/t_{GPL} = 10^3$ is a threshold for the dimension of GPL that

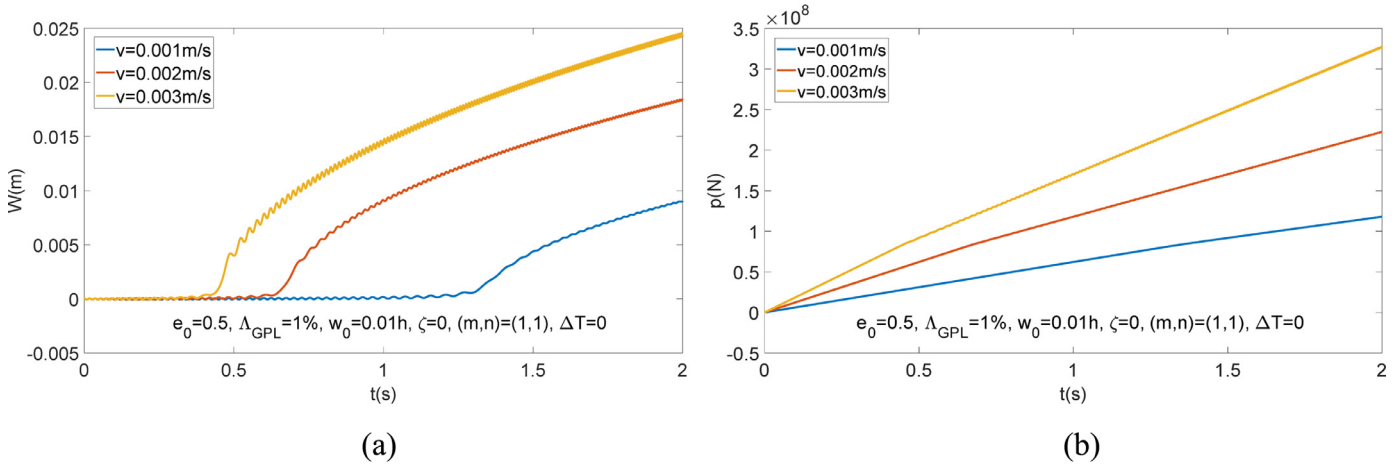

Fig. 10. (a) Deflections of the GPL-SFGP plate with various compressive loading velocities; (b) Buckling loads of the GPL-SFGP plate with various compressive loading velocities.

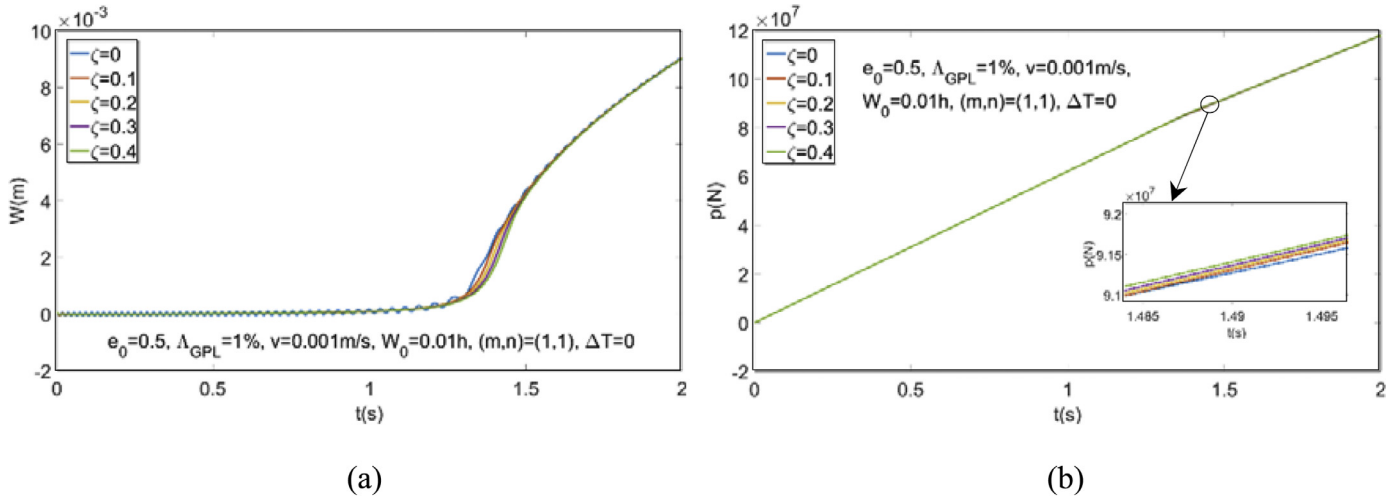

Fig. 11. (a) Deflections of the GPL-SFGP plate with various damping ratios; (b) Buckling loads of the GPL-SFGP plate with various damping ratios.

can be inserted for reducing the vibrational amplitude of the GPL-SFGP plate.

Moreover, as evidently illustrated in Fig. 9(c) and (d), for the same thickness of the GPLs, the increase of the length-to-width ratio of the GPL (i.e., $r_{l/w} = l_{GPL}/w_{GPL}$) leads to the increase of the amplitude of the vibration of the plate. This is due to the reduction of the surface area of the GPL when $r_{l/w}$ is increased.

5.3. Dynamic buckling analysis

In this subsection, the effects of the compressive loading velocity, damping ratio, temperature variation, initial imperfection, Winkler–Pasternak elastic foundation, porosity, GPL weight fraction, length-to-thickness ratio of the GPL, and length-to-width ratio of the GPL acting on the dynamic buckling behavior of the plate are thoroughly investigated. For a GPL-SFGP plate subjected to a compressive loading velocity, Eq. (71) is solved by the fourth-order Runge–Kutta method to investigate the nonlinear dynamic stability. The initial conditions are assumed to be $W(0) = W_0$, $\frac{dW}{dt}(0) = 0$. The Winkler–Pasternak elastic foundation coefficients are $k_w = 5 \times 10^4 \mathrm{N/m^2}$, $k_p = 5 \times 10^4 \mathrm{N/m}$.

Fig. 10(a) and (b) demonstrate the effect of the compressive loading velocity on the deflection and buckling load of the plate, respectively. With three different compressive loading velocities, namely v = 0.001m/s, 0.002m/s, 0.003m/s, the corresponding longitudinal end shortening of the plate can be obtained. As shown in Fig. 10(a), there are three distinct phases of the dynamic buckling curves, namely the slight fluctuation, the fast growth, and the eventual oscillation. With the increase of the compressive loading velocity, the slight fluctuation phase shortens significantly. Fig. 10(b) indicates that a higher velocity generally leads to a higher buckling load of the plate but with shorter reaching time.

The effect of the damping ratio on the dynamic buckling of the GPL-SFGP plate is presented in Fig. 11(a) and (b). The existence of damping ratio weakens the fluctuation of the plate while increasing the buckling load. Since the damped vibration is a process which depletes the system energy, so the increase of the damping ratio would accelerate the vibration attenuation.

Fig. 12(a) and (b) demonstrate the effect of the temperature variation on the dynamic buckling of the GPL-SFGP plate. Evidently, the enlargement of the temperature increment lengthens the slight fluctuation phase. However, the buckling load of the plate increases with the growth of the temperature increment.

The influence of the initial imperfection on the nonlinear dynamic buckling of the GPL-SFGP plate is indicated in the Fig. 13(a) and (b). Three sets of initial imperfection, namely W_0=0.1h, 0.01h, 0.001h, are selected in this study. It is noted that the increase of the initial imperfection shortens the slight fluctuation phase and reduces the buckling load of the plate.

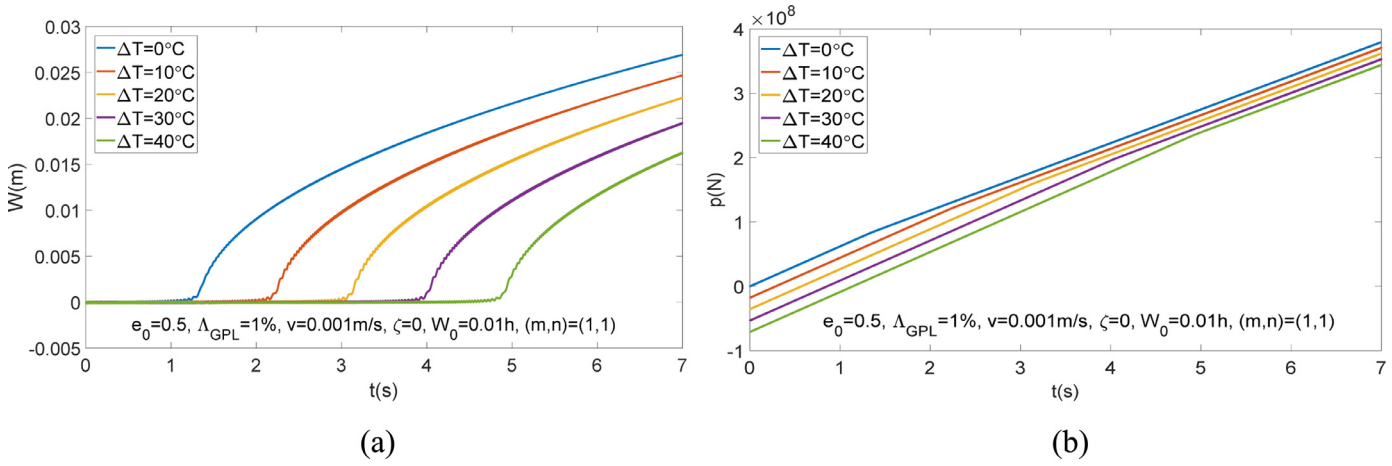

Fig. 12. (a) Deflections of the GPL-SFGP plate with various temperature increments; (b) Buckling loads of the GPL-SFGP plate with various temperature increments.

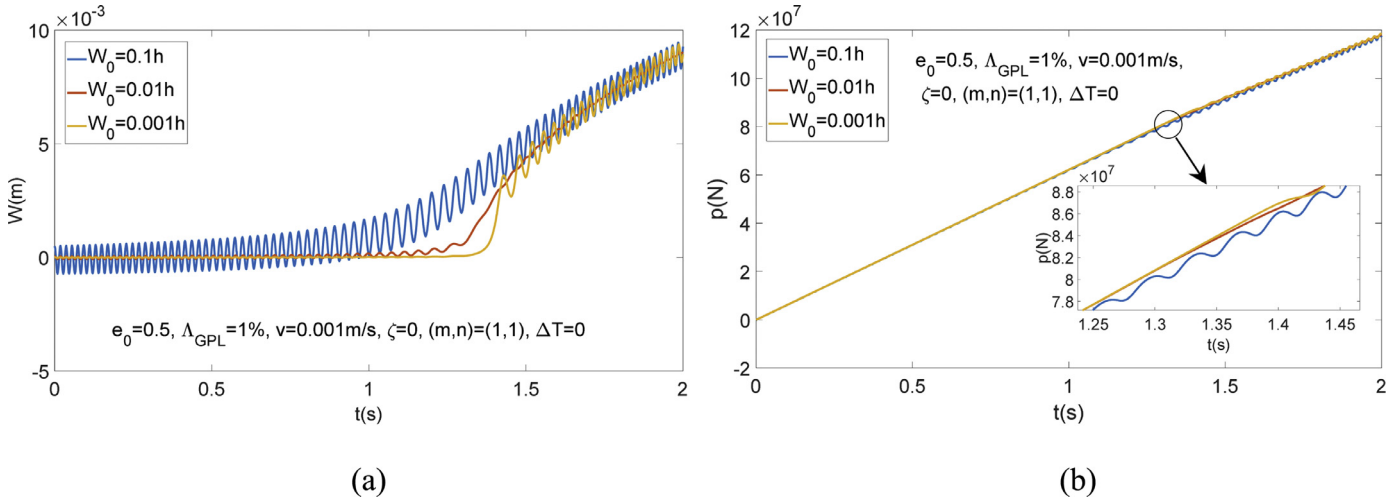

Fig. 13. (a) Deflections of the GPL-SFGP plate with various initial imperfections; (b) Buckling loads of the GPL-SFGP plate with various initial imperfections.

Fig. 14(a) and (b) illustrate the effect of various Winkler–Pasternak elastic foundation coefficients on the dynamic buckling of the plate. Clearly, the deflection of the plate decreases due to the existence of the Winkler–Pasternak elastic foundation, while the increase of the elastic foundation coefficients leads to the rise of the buckling load. The Pasternak coefficient is more pronounced than the Winkler one in terms of the impacts on the deflection as well as the buckling load, since the resistance provided by the Pasternak shear layer stiffness limits the lateral deflection of the plate.

The impact of different porosities of the porous core on the dynamic buckling of the plate are reported in Fig. 15(a) and (b). The larger value of the porosity means less metal matrix content, which results in the decrease of the density as well as the stiffness of the GPL-SFGP plate. Obviously, the increase of the porosity of the core prolongs the slight fluctuation phase of the plate. Also, in terms of the corresponding buckling loading showed in Fig. 15(b), the higher porosity of the GPL-SFGP plate, the smaller buckling load can be obtained.

The influence of various weight fractions of the GPL reinforcement on the dynamic buckling of the GPL-SFGP plate is illustrated in Fig. 16(a) and (b). It can be observed that increasing the weight percentage of the GPL within the GPL-SFGP plate results in the growth of the buckling load. Therefore, the buckling load of the plate can be increased by adding more GPLs into the porous core of the plate.

The influence of the dimensions of GPLs on the dynamic buckling behavior of the GPL- SFGP plate is indicated in Fig. 17. From Fig. 17(a) and (b), for the same width of GPLs, when the length-to-thick ratio of GPLs $r_{l/t}$ increases, the buckling load of the plate rises significantly. However, when the value of $r_{l/t}$ is larger than 10^3, the growth of the $r_{l/t}$ has no effect on the buckling load of the plate. Obviously, $r_{l/t}=10^3$ provides a threshold for the enhancement effect of the dimension of the GPLs on the dynamic stability of the plate. In terms of the impact of length-to-width ratio of the GPLs, as showed in Fig. 17(c) and (d), for the same thickness of the GPL, the higher value of $r_{l/w}$, the smaller dynamic buckling load can be gained.

6. Conclusion

This paper investigates the dynamic stability of a GPL-SFGP plate based on the classical plate theory by using an analytical approach. The Winkler–Pasternak elastic foundation, thermal and damping effects are taken into consideration during the analysis. In addition, some numerical simulations are presented to further explore the impacts of damping ratios, temperature increments, compressive loading velocities, the initial imperfections, elastic foundation parameters, porosities, GPL weight fractions and dimensions of GPLs. Some conclusions can be drawn from the presented analysis:

1. The damping ratio of the structure leads to slight decrease of the dynamic response and the dynamic buckling load of the plate due to the energy depletion.

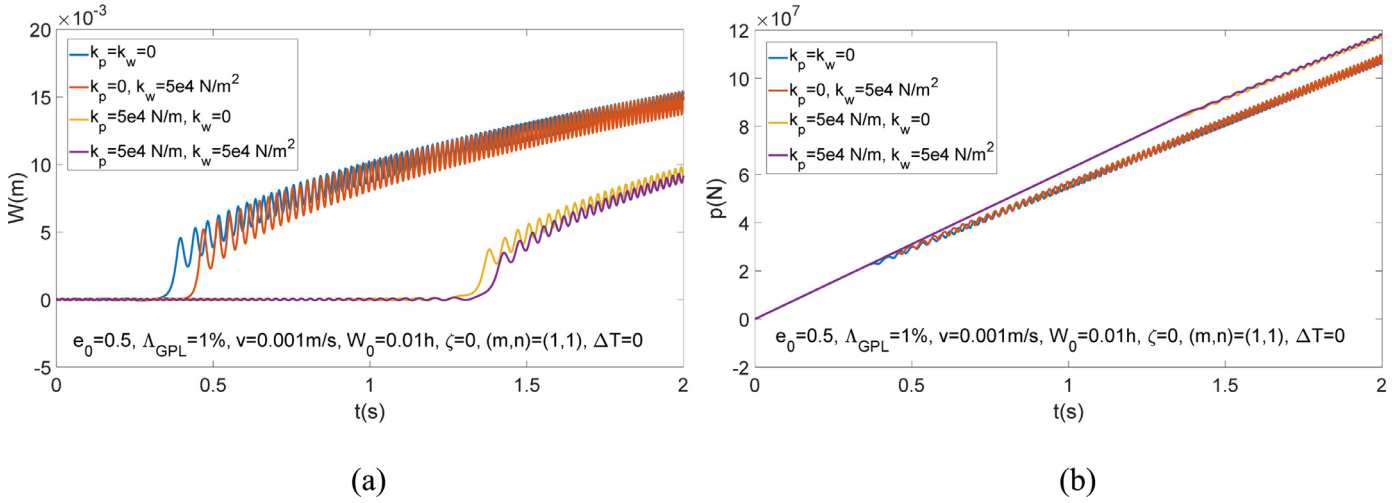

Fig. 14. (a) Deflections of the GPL-SFGP plate with various elastic foundation coefficients; (b) Buckling loads of the GPL-SFGP plate with various elastic foundation coefficients.

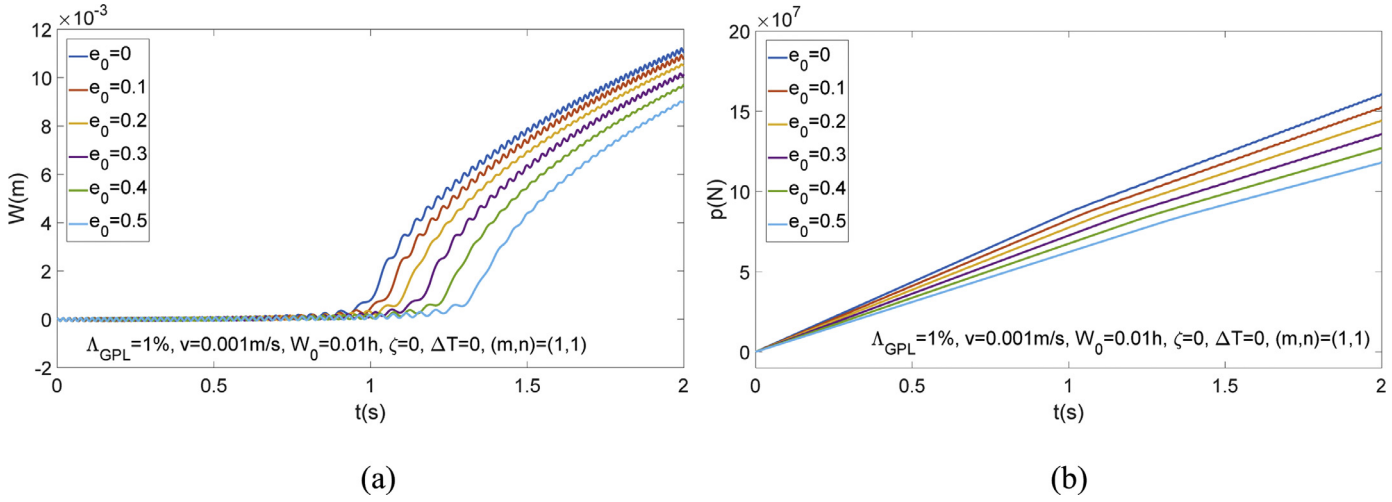

Fig. 15. (a) Deflection of the GPL-SFGP plate with various porosities; (b) Buckling loads of the GPL-SFGP plate with various porosities.

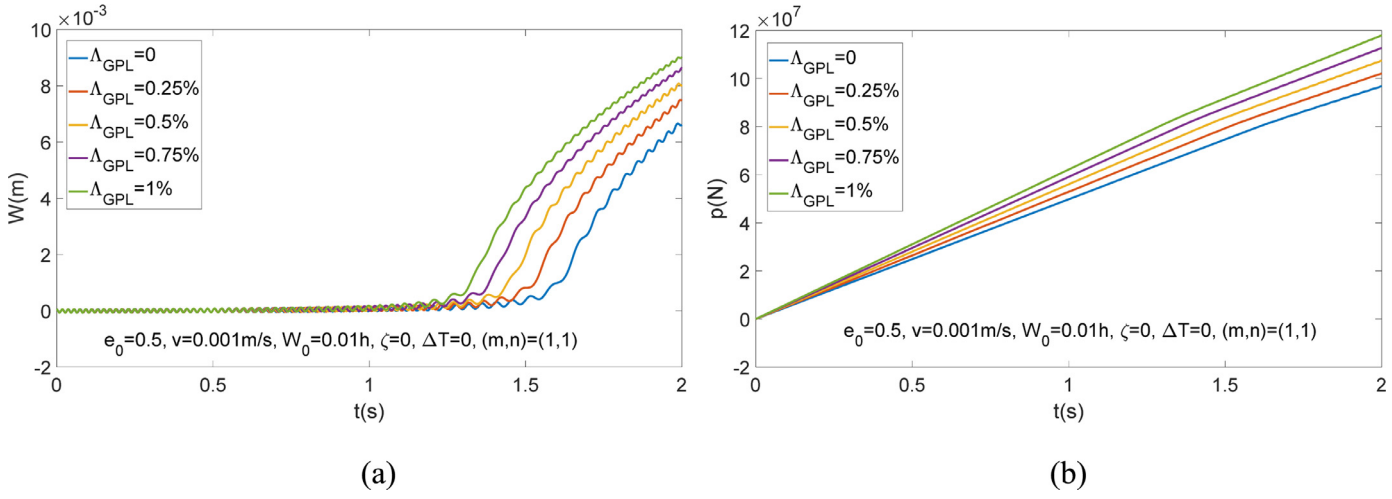

Fig. 16. (a) Deflections of the GPL-SFGP plate with various GPL weight fractions; (b) Buckling loads of the GPL-SFGP plate with various GPL weight fractions.

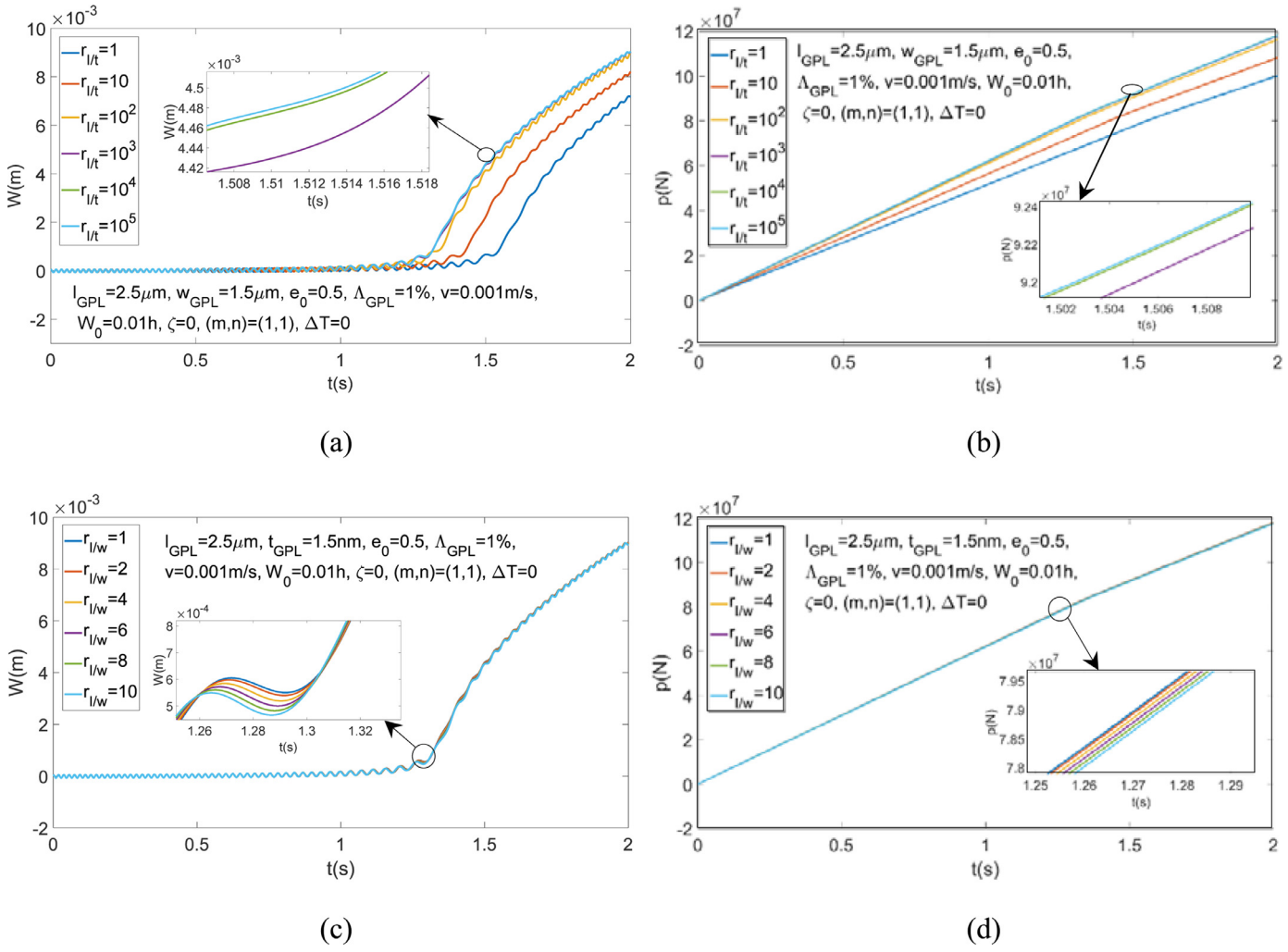

Fig. 17. (a) Deflections of the GPL-SFGP plate with various $r_{l/t}$; (b) Buckling loads of the GPL-SFGP plate with various $r_{l/t}$; (c) Deflections of the GPL-SFGP plate with various $r_{l/w}$; (d) Buckling loads of the GPL-SFGP plate with various $r_{l/w}$.

2. The initial imperfection of the plate causes the shortening of the slight fluctuation phase and the reduction of buckling load of the plate.
3. The temperature increment leads to a higher axial compressive stress when the edges of the plate are immovable. The rise of the environment temperature increment can depress the vibration of the plate, while increase the buckling load of the plate to some extent.
4. It is demonstrated that the supporting of the elastic foundation has beneficial effect on the nonlinear dynamic response of the plate. With the increase of the parameters of the Winkler–Pasternak foundation, the deflection of the plate can be decreased while the buckling load can be increased. It is noticed that the impact of the Pasternak shear layer stiffness is more significant than the Winkler one, which is demonstrated in both the nonlinear dynamic response and the dynamic buckling analyses of the plate.
5. The increase of the porosity of the porous core results in the reduction of the buckling load of the plate since both the stiffness and density of plate decrease.
6. The presence of the GPL reinforcement tends to increase the buckling load of the plate due to the improvement of the stiffness of the plate. However, such improvement is limited by a threshold value of 10^3 for the length-to-thickness ratio of GPLs.

Acknowledgment

The work presented in this paper has been supported by Australian Research Council projects DP160103919 and IH150100006.

References

[1] Birman V, Kardomateas GA. Review of current trends in research and applications of sandwich structures. Compos Part B: Eng 2018;142:221–40. doi:10.1016/J.COMPOSITESB.2018.01.027.
[2] Carlsson LA, Kardomateas GA. Structural and failure mechanics of sandwich composites, 121. Netherlands: Dordrecht: Springer; 2011. doi:10.1007/978-1-4020-3225-7.
[3] Vinson JR. Sandwich structures: past, present, and future. sandwich structures. 7: Advancing with sandwich structures and materials. Berlin/Heidelberg: Springer-Verlag; 2005. p. 3–12. doi:10.1007/1-4020-3848-8_1.
[4] Sofiyev AH. Application of the FOSDT to the solution of buckling problem of FGM sandwich conical shells under hydrostatic pressure. Compos Part B: Eng 2018;144:88–98. doi:10.1016/J.COMPOSITESB.2018.01.025.
[5] Kolahchi R, Zarei MS, Hajmohammad MH, Nouri A. Wave propagation of embedded viscoelastic FG-CNT-reinforced sandwich plates integrated with sensor and actuator based on refined zigzag theory. Int J Mech Sci 2017;130:534–45. doi:10.1016/J.IJMECSCI.2017.06.039.
[6] Kolahchi R. A comparative study on the bending, vibration and buckling of viscoelastic sandwich nano-plates based on different nonlocal theories using DC, HDQ and DQ methods. Aerosp Sci Technol 2017;66:235–48. doi:10.1016/J.AST.2017.03.016.
[7] Arani AG, Jafari GS, Kolahchi R. Nonlinear vibration analysis of viscoelastic micro nano-composite sandwich plates integrated with sensor and actuator. Microsyst Technol 2017;23:1509–35. doi:10.1007/s00542-016-3095-9.

[8] Sofiyev AH. The vibration and buckling of sandwich cylindrical shells covered by different coatings subjected to the hydrostatic pressure. Compos Struct 2014;117:124–34. doi:10.1016/J.COMPSTRUCT.2014.06.025.
[9] Sofiyev AH. The stability analysis of shear deformable FGM sandwich conical shells under the axial load. Compos Struct 2017;176:803–11. doi:10.1016/J.COMPSTRUCT.2017.06.022.
[10] Ashby MF. Metal foams : a design guide. Butterworth-Heinemann; 2000.
[11] Banhart J. Manufacture, characterisation and application of cellular metals and metal foams. Prog Mater Sci 2001;46:559–632. doi:10.1016/S0079-6425(00)00002-5.
[12] Ramamurty U, Paul A. Variability in mechanical properties of a metal foam. Acta Mater 2004;52:869–76. doi:10.1016/J.ACTAMAT.2003.10.021.
[13] Miyoshi T, Itoh M, Akiyama S, Kitahara A. ALPORAS aluminum foam: production process, properties, and applications. Adv Eng Mater 2000;2:179–83. doi:10.1002/(SICI)1527-2648(200004)2:4<179::AID-ADEM179>3.0.CO;2-G.
[14] Lind-Nordgren E, Göransson P. Optimising open porous foam for acoustical and vibrational performance. J Sound Vib 2010;329:753–67. doi:10.1016/J.JSV.2009.10.009.
[15] Liu C, Zhang YX, Yang C. Numerical modelling of mechanical behaviour of aluminium foam using a representative volume element method. Int J Mech Sci 2016;118:155–65. doi:10.1016/j.ijmecsci.2016.08.021.
[16] Radford DD, McShane GJ, Deshpande VS, Fleck NA. The response of clamped sandwich plates with metallic foam cores to simulated blast loading. Int J Solids Struct 2006;43:2243–59. doi:10.1016/j.ijsolstr.2005.07.006.
[17] Pollien A, Conde Y, Pambaguian L, Mortensen A. Graded open-cell aluminium foam core sandwich beams. Mater Sci Eng: A 2005;404:9–18. doi:10.1016/J.MSEA.2005.05.096.
[18] Banhart J, Seeliger H-W. Aluminium Foam Sandwich Panels: Manufacture, Metallurgy and Applications. Adv Eng Mater 2008;10:793–802. doi:10.1002/adem.200800091.
[19] Hou W, Zhu F, Lu G, Fang Dd-N. Ballistic impact experiments of metallic sandwich panels with aluminium foam core. Int J Impact Eng 2010;37:1045–55. doi:10.1016/j.ijimpeng.2010.03.006.
[20] Magnucka-Blandzi E. Dynamic stability and static stress state of a sandwich beam with a metal foam core using three modified timoshenko hypotheses. Mech Adv Mater Struct 2011;18:147–58. doi:10.1080/15376494.2010.496065.
[21] Crupi V, Montanini R. Aluminium foam sandwiches collapse modes under static and dynamic three-point bending. Int J Impact Eng 2007;34:509–21. doi:10.1016/J.IJIMPENG.2005.10.001.
[22] Qin Q, Zheng X, Zhang J, Yuan C, Wang TJ. Dynamic response of square sandwich plates with a metal foam core subjected to low-velocity impact. Int J Impact Eng 2018;111:222–35. doi:10.1016/J.IJIMPENG.2017.09.011.
[23] Banhart J, García-Moreno F, Heim K, Seeliger H-W. Light-weighting in transportation and defence using aluminium foam sandwich structures. 2017.
[24] Thailand Planning Chinese-Made High-Speed Railway Systems – Chiang Rai Times English News Paper n.d. https://www.chiangraitimes.com/thailand-planning-chinese-made-high-speed-railway-systems.html (accessed August 31, 2018).
[25] Iijima S. Helical microtubules of graphitic carbon. Nature 1991;354:56–8. doi:10.1038/354056a0.
[26] Imani Yengejeh S, Kazemi SA, Öchsner A. Carbon nanotubes as reinforcement in composites: a review of the analytical, numerical and experimental approaches. Comput Mater Sci 2017;136:85–101. doi:10.1016/J.COMMATSCI.2017.04.023.
[27] Mehar K, Panda SK, Mahapatra TR. Theoretical and experimental investigation of vibration characteristic of carbon nanotube reinforced polymer composite structure. Int J Mech Sci 2017;133:319–29. doi:10.1016/j.ijmecsci.2017.08.057.
[28] Kolahchi R, Moniri Bidgoli AM. Size-dependent sinusoidal beam model for dynamic instability of single-walled carbon nanotubes. Appl Math Mech 2016;37:265–74. doi:10.1007/s10483-016-2030-8.
[29] Mittal G, Dhand V, Rhee KY, Park S-J, Lee WR. A review on carbon nanotubes and graphene as fillers in reinforced polymer nanocomposites. J Ind Eng Chem 2015;21:11–25. doi:10.1016/J.JIEC.2014.03.022.
[30] Young RJ, Kinloch IA, Gong L, Novoselov KS. The mechanics of graphene nanocomposites: a review. Compos Sci Technol 2012;72:1459–76. doi:10.1016/j.compscitech.2012.05.005.
[31] Rafiee MA, Rafiee J, Wang Z, Song H, Yu Z-Z, Koratkar N. Enhanced mechanical properties of nanocomposites at low graphene content. ACS Nano 2009;3:3884–90. doi:10.1021/nn9010472.
[32] Zaman I, Kuan H-C, Dai J, Kawashima N, Michelmore A, Sovi A, et al. From carbon nanotubes and silicate layers to graphene platelets for polymer nanocomposites. Nanoscale 2012;4:4578. doi:10.1039/c2nr30837a.
[33] Sofiyev AH, Kuruoglu N. Parametric instability of shear deformable sandwich cylindrical shells containing an FGM core under static and time dependent periodic axial loads. Int J Mech Sci 2015;101–102:114–23. doi:10.1016/J.IJMECSCI.2015.07.025.
[34] Yang J, Wu H, Kitipornchai S. Buckling and postbuckling of functionally graded multilayer graphene platelet-reinforced composite beams. Compos Struct 2017;161:111–18. doi:10.1016/j.compstruct.2016.11.048.
[35] Sofiyev AH, Hui D, Najafov AM, Turkaslan S, Dorofeyskaya N, Yuan GQ. Influences of shear stresses and rotary inertia on the vibration of functionally graded coated sandwich cylindrical shells resting on the Pasternak elastic foundation. J Sandw Struct Mater 2015;17:691–720. doi:10.1177/1099636215594560.
[36] Chen D, Yang J, Kitipornchai S. Free and forced vibrations of shear deformable functionally graded porous beams. Int J Mech Sci 2016;108–109:14–22. doi:10.1016/j.ijmecsci.2016.01.025.
[37] Chen D, Kitipornchai S, Yang J. Nonlinear free vibration of shear deformable sandwich beam with a functionally graded porous core. Thin-Walled Struct 2016;107:39–48. doi:10.1016/j.tws.2016.05.025.
[38] Wu D, Liu A, Huang Y, Huang Y, Pi Y, Gao W. Dynamic analysis of functionally graded porous structures through finite element analysis. Eng Struct 2018;165:287–301. doi:10.1016/J.ENGSTRUCT.2018.03.023.
[39] Chen D, Kitipornchai S, Yang J. Dynamic response and energy absorption of functionally graded porous structures. Mater Des 2018;140:473–87. doi:10.1016/J.MATDES.2017.12.019.
[40] Kitipornchai S, Chen D, Yang J. Free vibration and elastic buckling of functionally graded porous beams reinforced by graphene platelets. Mater Des 2017;116:656–65. doi:10.1016/j.matdes.2016.12.061.
[41] Chen D, Yang J, Kitipornchai S. Nonlinear vibration and postbuckling of functionally graded graphene reinforced porous nanocomposite beams. Compos Sci Technol 2017;142:235–45. doi:10.1016/J.COMPSCITECH.2017.02.008.
[42] Sahmani S, Aghdam MM, Rabczuk T. Nonlinear bending of functionally graded porous micro/nano-beams reinforced with graphene platelets based upon nonlocal strain gradient theory. Compos Struct 2018;186:68–78. doi:10.1016/j.compstruct.2017.11.082.
[43] Yang J, Chen D, Kitipornchai S. Buckling and free vibration analyses of functionally graded graphene reinforced porous nanocomposite plates based on Chebyshev-Ritz method. Compos Struct 2018;193:281–94. doi:10.1016/J.COMPSTRUCT.2018.03.090.
[44] Dong YH, Li YH, Chen D, Yang J. Vibration characteristics of functionally graded graphene reinforced porous nanocomposite cylindrical shells with spinning motion. Compos Part B: Eng 2018;145:1–13. doi:10.1016/J.COMPOSITESB.2018.03.009.
[45] Aksogan O, Sofiyev AH. Dynamic buckling of a cylindrical shell with variable thickness subject to a time-dependent external pressure varying as a power function of time. J Sound Vib 2002;254:693–702. doi:10.1006/JSVI.2001.4115.
[46] Deniz A, Sofiyev AH. The nonlinear dynamic buckling response of functionally graded truncated conical shells. J Sound Vib 2013;332:978–92. doi:10.1016/J.JSV.2012.09.032.
[47] Huang H, Han Q. Nonlinear dynamic buckling of functionally graded cylindrical shells subjected to time-dependent axial load. Compos Struct 2010;92:593–8. doi:10.1016/J.COMPSTRUCT.2009.09.011.
[48] Sofiyev AH. On the dynamic buckling of truncated conical shells with functionally graded coatings subject to a time dependent axial load in the large deformation. Compos Part B: Eng 2014;58:524–33. doi:10.1016/J.COMPOSITESB.2013.10.013.
[49] Mouhat O, Abdellatif K. Dynamic buckling of stiffened panels. Procedia Eng 2015;125:1001–7. doi:10.1016/J.PROENG.2015.11.154.
[50] Ramezannezhad Azarboni H, Darvizeh M, Darvizeh A, Ansari R. Nonlinear dynamic buckling of imperfect rectangular plates with different boundary conditions subjected to various pulse functions using the Galerkin method. Thin-Walled Struct 2015;94:577–84. doi:10.1016/J.TWS.2015.04.002.
[51] Kolahchi R, Safari M, Esmailpour M. Dynamic stability analysis of temperature-dependent functionally graded CNT-reinforced visco-plates resting on orthotropic elastomeric medium. Compos Struct 2016;150:255–65. doi:10.1016/J.COMPSTRUCT.2016.05.023.
[52] Yang B, Wang D. Dynamic buckling of stiffened plates with elastically restrained edges under in-plane impact loading. Thin-Walled Struct 2016;107:427–42. doi:10.1016/J.TWS.2016.06.019.
[53] Sheng GG, Wang X. Nonlinear vibrations of FG cylindrical shells subjected to parametric and external excitations. Compos Struct 2018;191:78–88. doi:10.1016/j.compstruct.2018.02.018.
[54] Hajmohammad MH, Zarei MS, Nouri A, Kolahchi R. Dynamic buckling of sensor/functionally graded-carbon nanotube-reinforced laminated plates/actuator based on sinusoidal-visco-piezoelasticity theories. J Sandw Struct Mater 2017:109963621772037. doi:10.1177/1099636217720373.
[55] Gao K, Gao W, Wu D, Song C. Nonlinear dynamic characteristics and stability of composite orthotropic plate on elastic foundation under thermal environment. Compos Struct 2017;168:619–32. doi:10.1016/j.compstruct.2017.02.054.
[56] Hajmohammad MH, Azizkhani MB, Kolahchi R. Multiphase nanocomposite viscoelastic laminated conical shells subjected to magneto-hygrothermal loads: dynamic buckling analysis. Int J Mech Sci 2018;137:205–13. doi:10.1016/J.IJMECSCI.2018.01.026.
[57] Ghorbanpour Arani A, Khani M, Khoddami Maraghi Z. Dynamic analysis of a rectangular porous plate resting on an elastic foundation using high-order shear deformation theory. J Vib Control 2017;24:3698–713. doi:10.1177/1077546317709388.
[58] Fakhar A, Kolahchi R. Dynamic buckling of magnetorheological fluid integrated by visco-piezo-GPL reinforced plates. Int J Mech Sci 2018;144:788–99. doi:10.1016/J.IJMECSCI.2018.06.036.
[59] Halpin JC, Louis S, Kardos JL. The Halpin-Tsai equations: a review. Polym Eng Sci 1976;16:344–52.
[60] Guzmán de Villoria R, Miravete A. Mechanical model to evaluate the effect of the dispersion in nanocomposites. Acta Mater 2007;55:3025–31. doi:10.1016/J.ACTAMAT.2007.01.007.
[61] Shokrieh MM, Esmkhani M, Shokrieh Z, Zhao Z. Stiffness prediction of graphene nanoplatelet/epoxy nanocomposites by a combined molecular dynamics–micromechanics method. Comput Mater Sci 2014;92:444–50. doi:10.1016/J.COMMATSCI.2014.06.002.
[62] EKSTROM RE. Dynamic buckling of a rectangular orthotropic plate. AIAA J 1973;11:1655–9. doi:10.2514/3.50665.